Accepted Manuscript

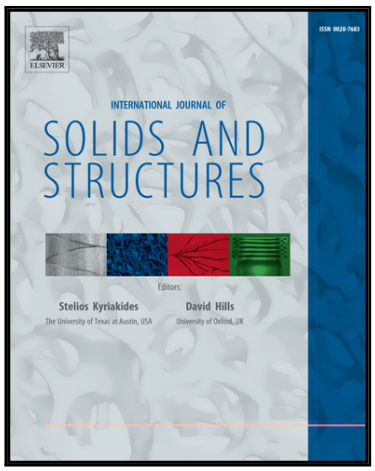

Experimental Fracture Characterization of an Anisotropic Magnesium Alloy Sheet in Proportional and Non-Proportional Loading Conditions

A. Abedini , C. Butcher , M.J. Worswick

PII: S0020-7683(18)30154-9
DOI: 10.1016/j.ijsolstr.2018.04.010
Reference: SAS 9965

To appear in: *International Journal of Solids and Structures*

Received date: 24 November 2017
Revised date: 3 April 2018
Accepted date: 8 April 2018

Please cite this article as: A. Abedini , C. Butcher , M.J. Worswick , Experimental Fracture Characterization of an Anisotropic Magnesium Alloy Sheet in Proportional and Non-Proportional Loading Conditions, *International Journal of Solids and Structures* (2018), doi: 10.1016/j.ijsolstr.2018.04.010

Experimental Fracture Characterization of an Anisotropic Magnesium Alloy Sheet in Proportional and Non-Proportional Loading Conditions

A. Abedini*, C. Butcher, M.J. Worswick

Department of Mechanical and Mechatronics Engineering, University of Waterloo, Waterloo, ON, CANADA

*Corresponding author. Email: aabedini@uwaterloo.ca

Abstract: A comprehensive experimental investigation was performed to characterize the fracture behaviour of a rare-earth magnesium alloy sheet, ZEK100-O, under both proportional and non-proportional loading conditions. This material possesses severe plastic anisotropy and tension-compression asymmetry that evolve with plastic deformation and is an excellent candidate to experimentally evaluate phenomenological fracture modelling strategies. Different types of specimen geometries were fabricated in different orientations with respect to the rolling direction of the sheet to reveal the anisotropic fracture response of the alloy. Moreover, three different types of plane-strain tension tests, namely, v-bend, butterfly, and Nakazima dome tests were conducted and compared in terms of their applicability for fracture characterization of sheet materials. To visualize directional dependency of the fracture response of the magnesium alloy, experimental fracture *loci* for different orientations were constructed. Furthermore, non-proportional tests were performed in which abrupt changes in stress state were imposed to study the role of the loading history on fracture behaviour of the alloy. The non-proportional tests entailed pre-straining the material in uniaxial and equi-biaxial tension up to a prescribed plastic work level, followed by extreme strain path changes to plane-strain tension and shear states. Non-proportional deformations with such severe strain path variations have not been reported in the literature for materials with complex anisotropic behaviour such as ZEK100-O. The results of which have enabled the direct experimental evaluation of phenomenological damage models without performing an inverse calibration from finite element simulations. Based on the results of the non-proportional tests, it was shown that simple damage indicators were unable to describe the influence of severe changes in the strain path on fracture.

Keywords: Fracture characterization, magnesium alloy, non-proportional loading, damage accumulation

1. Introduction

Motivated by increasing demand to reduce vehicle weight by incorporating lightweight materials, research on magnesium alloys has been receiving significant attention from the automotive industry. However, despite a high strength-to-weight ratio, applications of wrought magnesium alloys are limited due to insufficient formability at room temperature, pronounced anisotropic response, and poor corrosion resistance (Zarandi and Yue, 2011). To address these issues, the addition of rare-earth elements emerged as a potential solution to increase formability while preserving the low density of magnesium alloys (Imandoust *et al.*, 2017). Nevertheless, severe anisotropy persists in rare-earth magnesium and from the perspective of evolution of anisotropy and complications in plasticity and fracture, behaviour of such materials is even more complex than conventional commercial magnesium alloys such as AZ31B (Kurukuri *et al.*, 2014; Abedini *et al.*, 2017a). Therefore, these alloys require a broad material characterization to develop and calibrate anisotropic constitutive plasticity and fracture models.

Notable progress has been made over the past two decades in developing and modifying robust experimental methods to characterize the effect of stress state on fracture initiation in sheet metals over a wide range of stress triaxialities. For instance, significant efforts have been made to design shear specimens to evaluate the fracture response under zero hydrostatic stress and stress triaxiality (Mohr and Henn, 2007; Tarigopula *et al.*, 2008; Peirs *et al.*, 2012). In addition, characterization tests by flat specimens with central holes or notches have been widely used to study the failure behaviour under tensile dominated stress states (Bao, 2004; Luo *et al.*, 2012; Roth and Mohr, 2016). The critical plane-strain tension state has been achieved using specimens featuring wide gauge widths to supresses straining in the width direction (Mohr and Henn, 2007; Flores *et al.*, 2010; Bagheriasl and Worswick, 2015; Cheong *et al.*, 2017). Moreover, Nakazima dome and bulge tests have been utilized as candidate experimental techniques to determine equi-biaxial tension behaviour of sheets (Bai and Wierzbicki, 2010; Koc *et al.*, 2011). Using these experimental techniques, fracture strains under a wide range of stress states can be governed leading to a better understanding of the fracture behaviour of sheet metals.

The interest in developing improved characterization tests for proportional loading conditions has been driven by the adoption of phenomenological fracture models that are stress state

dependent such as the modified Mohr-Coulomb (MMC) (Bai and Wierzbicki, 2010), Lou-Huh (Lou and Huh, 2013), and Hosford-Coulomb (Mohr and Marcadet, 2015) as notable examples. In this modelling framework, proportional characterization tests are performed followed by extensive numerical modelling of each characterization test to obtain local stress and strain histories. The stress history, that can be quite non-linear due to localization in tensile-based coupons such as in notched tensile tests, is then averaged into an "average stress triaxiality" for model calibration with the failure strains. Alternatively, an optimization code can be used to integrate the numerical stress path with a damage parameter, D, that predicts fracture when D=1. However, Benzerga *et al*. (2012) correctly pointed out that there are infinite ways to average the stress triaxiality and that the failure strain will be different due to microstructure evolution in non-linear strain paths even if the average triaxiality is constant. For example, a two-stage deformation path of uniaxial tensile loading followed by uniaxial compression back to the initial length would lead to an average stress triaxiality of zero which corresponds to a shear state.

Nevertheless, phenomenological failure models are straightforward to use and perform much better than expected in forming (*e.g.* Malcher *et al*., 2012; Anderson *et al*., 2017) and crash simulations (*e.g.* Omer *et al*., 2017) that is a testament to their widespread adoption. However, there is a clear need to experimentally evaluate the influence of non-proportionality on the fracture behaviour and assess the predictions of a phenomenological damage model, especially for an anisotropic material such as magnesium alloys. In the so-called "hybrid experimental-numerical" approach to fracture characterization, the failure model is generated from the simulations of the experiments and the procedure is effectively a closed-loop validation which is a prime reason that different phenomenological models can be calibrated to give similar results despite different formulations.

In addition, understanding of the behaviour of materials under non-proportional states is essential since in forming operations and in crash events, materials are subjected to complex stress state changes. The role of non-proportionality on yielding behaviour of materials is well-established with concepts of kinematic hardening (Chaboche, 2008) and distortional hardening in homogeneous anisotropic hardening (HAH) models (Barlat *et al.*, 2011; 2017). Moreover, it is well-known that the onset of necking is dependent on the loading history of sheet metals (Volk and Suh, 2013; Jocham *et al.*, 2016). Graf and Hosford (1993) showed that pre-straining an

AA2008-T4 alloy remarkably influenced its forming limit diagram (FLD). A similar observation on path-dependency of FLDs was made by Korkolis and Kyriakides (2009) for AA6260-T4 tubes under combined internal pressure and axial loading. To overcome this issue, Stoughton (2000) proposed a stress-based FLD that significantly reduced path-dependency of forming limit curves (see also Stoughton and Yoon, 2012); however, it was discussed by Yoshida and Kuwabara (2007) that the idea of stress-based FLDs is strictly valid for isotropic hardening models while non-isotropic hardening effects are only manifested in non-proportional loading.

In contrast to the published research on the role of non-proportionality on yielding response and FLDs, there are limited studies on fracture characterization of materials under non-proportional conditions. Bao and Treitler (2004) performed notch compression tests on axisymmetric AA2024-T351 bars followed by tension tests to fracture where a substantial increase in ductility was reported due to the pre-straining in compression. Basu and Benzerga (2015) studied a conventional medium-carbon steel alloy by uniaxial tension with axisymmetric bars followed by machining notches on the specimen to increase the stress triaxiality. In addition, the influence of the loading direction reversal on the onset of fracture of DP780 steel sheet was investigated by Marcadet and Mohr (2015) through compression-tension experiments where it was reported that the strain to fracture was increased with pre-straining in compression. A similar study was also performed by Papasidero *et al*. (2015) on AA2024-T351 tubes by pre-straining the material in tension, compression, and torsion where it was observed that applying pre-compression and pre-torsion increased the ductility while applying pre-tension reduced the ductility of the material. More recently, ten Kortenaar (2016) studied the influence of non-proportional loadings on fracture behaviour of boron steel under different loading conditions after imposing an initial biaxial pre-straining.

The objective of the present work is to experimentally characterize fracture behaviour of a rare-earth magnesium alloy, ZEK100-O, under proportional and non-proportional loading conditions. The fracture response of ZEK100-O has not been thoroughly studied in the literature, even under proportional loading, the notable exception being the microstructural study of Ray and Wilkinson (2016) in which the failure behaviour of ZEK100-O was analyzed with notched tensile specimens where the role of grain boundaries and twin boundaries on fracture initiation was revealed. The formability of this material has been studied by Boba *et al*. (2017) for a range

of temperatures, who reported significant anisotropy in the forming limit strains, particularly at room temperature. However, formability is typically controlled by the onset of necking whereas the current paper focuses on strain at final fracture. To the authors' knowledge, magnesium alloys have not been investigated in terms of their fracture behaviour under non-proportional loading conditions. Unlike most of the studies cited above in which only a uniaxial state is applied for pre-straining (of steel and aluminum sheets), the present study will consider both uniaxial and equi-biaxial tension states with dogbone and Marciniak tests, respectively, for the initial stages of deformation of the magnesium alloy, followed by simple shear and plane-strain tension conditions up to fracture.

To these ends, a novel test program was undertaken to experimentally obtain the fracture strains in proportional plane-stress loading conditions and to calibrate a phenomenological damage model. Secondly, a series of severely non-proportional loading conditions were achieved where the pre-straining tests enable experimental assessments of non-proportional stress states as shear and tight-radius bending samples were extracted from the deformed region where homogeneous plane-stress conditions apply. Furthermore, the magnitude of pre-straining in the various tests was performed up to the same level of plastic work to enable an appropriate comparison between stress states; such an approach has not been considered in prior non-proportional experimental studies. Therefore, it is expected that the present study would shed some light into the understanding of fracture in magnesium alloys under various proportional and non-proportional loading conditions.

2. Material

The material used in the present study was a commercial rare-earth magnesium alloy, ZEK100 (O-temper) rolled sheet with a nominal thickness of 1.55 mm. Recently, Abedini *et al.* (2017a) performed X-Ray Diffraction (XRD) analysis on this same lot of material and reported that the texture of ZEK100-O exhibits a spread of the basal poles along the transverse direction which is typical of rare-earth magnesium rolled sheets (Figure 1). The engineering stress-strain response of the material in uniaxial tension was obtained with a sub-sized ASTM E8 specimen under a quasi-static strain rate of 0.001 s^{-1}, with specimens extracted from the rolling (RD),

diagonal (DD), and transverse (TD) directions of the sheet. As shown in Figure 2a, the material demonstrates significant anisotropic behaviour with the rolling direction having the highest ultimate tensile strength (UTS). Furthermore, the variation in the instantaneous r-values (Lankford parameters) depicted in Figure 2(b) suggests evolution of the texture of the material with deformation and highlights the complexities associated with constructing yield *loci* for the material.

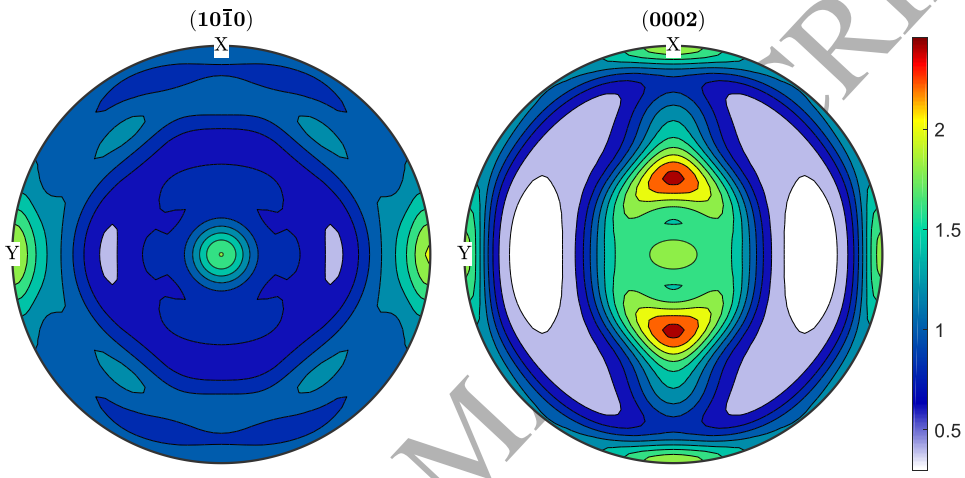

Figure 1 – XRD pole figures for as-received ZEK100-O sheet. X and Y directions correspond to the TD and RD, respectively.

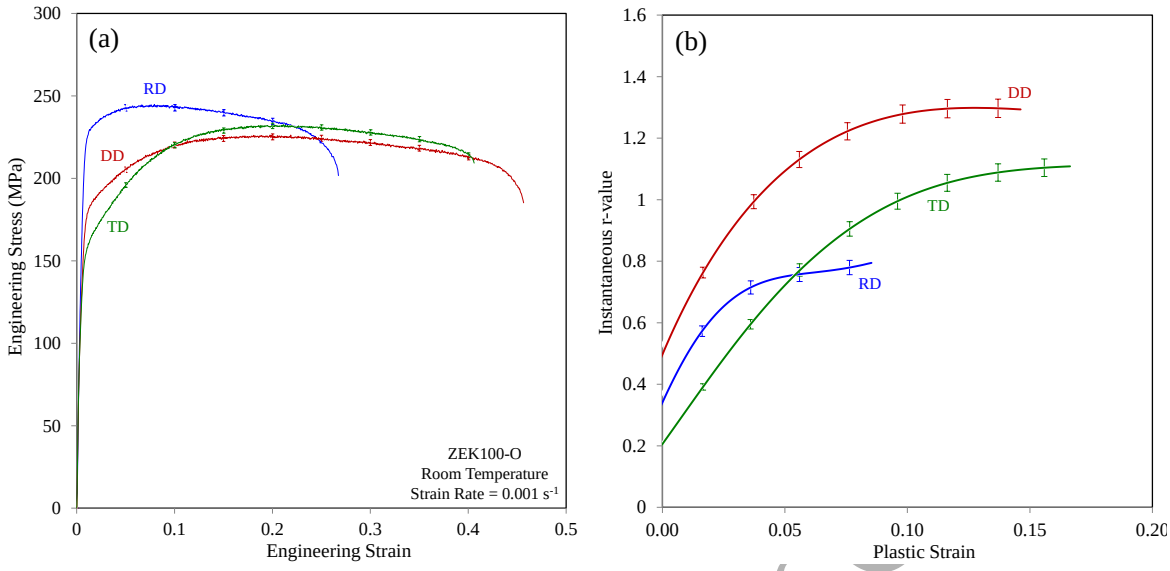

Figure 2 – Uniaxial tensile response obtained with sub-sized ASTM E8 specimens tested at room temperature under a quasi-static strain rate of 0.001 s^{-1} in terms of (a) engineering stress-strain curves and (b) instantaneous r-values.

The constitutive response of this material under a wide range of stress states was reported by Abedini *et al.* (2017a). Recently, Abedini *et al.* (2017d) used this experimental data to calibrate the CPB06 yield criterion of Cazacu *et al.* (2006) at different levels of plastic deformation and the yield *loci* for two of these plastic deformation levels, *i.e.* the plastic work levels of 2.24 MJ/m^3 and 22.46 MJ/m^3 (associated with equivalent plastic strains of 0.01 and 0.09 for a uniaxial tension test in the RD), are presented in Figure 3. Note that the specific plastic work, w_p, is defined as:

$$w_p = \int \boldsymbol{\sigma} : d\boldsymbol{\varepsilon}^p \tag{1}$$

where $\boldsymbol{\sigma}$ and $d\boldsymbol{\varepsilon}^p$ are the stress and plastic strain rate tensors, respectively. It can be seen from Figure 3 that ZEK100-O displays a significant tension-compression asymmetry. For the lower plastic work level of 2.24 MJ/m^3, which is close to initial yielding, it can be seen from Figure 3(a) that the tension region (first quadrant) exhibits larger yield stresses than the compression region (third quadrant), however this trend is reversed at the plastic work level of 22.46 MJ/m^3 in Figure 3(b). Therefore, it is apparent that the shape of the yield *loci* of ZEK100-O evolves with

deformation. The experimental results presented in Figures 2 and 3 show the challenging nature of ZEK100-O in terms of constitutive characterization.

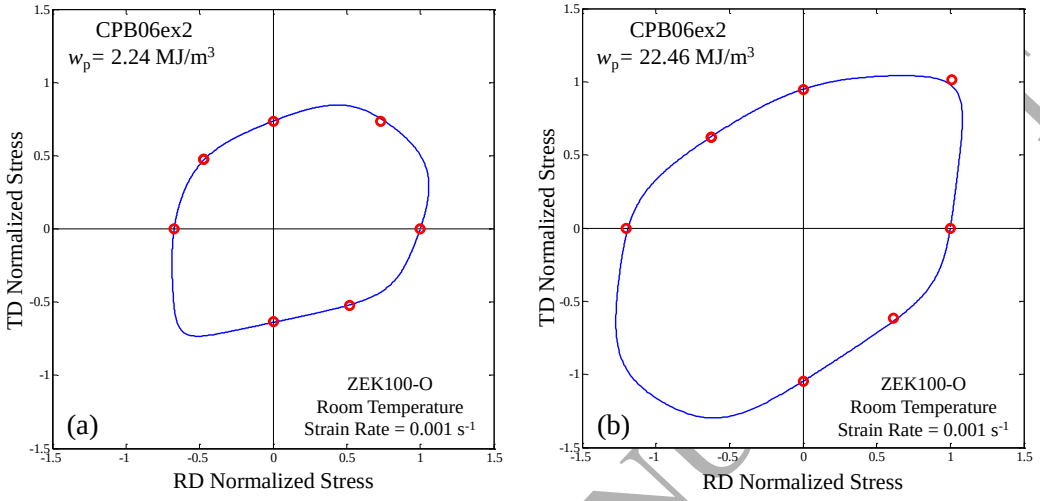

Figure 3 – Yield *loci* of ZEK100-O with CPB06ex2 formulation obtained from Abedini *et al*. (2017d) calibrated at two plastic work levels of (a) 2.24 MJ/m^3 and (b) 22.46 MJ/m^3. It should be mentioned that the plastic work levels of 2.24 MJ/m^3 and 22.46 MJ/m^3 correspond to equivalent plastic strains of 0.01 and 0.09, respectively, for a uniaxial tension test in the reference direction of the RD.

3. Experiments and methodology

Different types of experimental tests were performed in the present study to evaluate the fracture behaviour of ZEK100-O sheet at room temperature under quasi-static conditions. In terms of the loading histories, these tests can be categorized into two types, corresponding to "proportional" *versus* "non-proportional" conditions. This section describes the experiments along with the strain measurement techniques used to obtain fracture strains under different loading conditions. It is common in the literature to define the stress state in terms of the stress triaxiality and Lode parameter; thus before describing the tests, these concepts in characterization of loading conditions with stress invariant are reviewed.

3.1. Characterization of stress state

The first invariant of the stress tensor, I_1, and the second and third invariant of the stress deviator, J_2 and J_3, are defined as:

$$I_1 = tr(\boldsymbol{\sigma}),\ J_2 = \frac{1}{2}(\boldsymbol{s}:\boldsymbol{s}),\ J_3 = \det(\boldsymbol{s}) \quad (2,3,4)$$

where $\boldsymbol{s}$ is the stress deviator. Note that boldface letters refer to tensor quantities and the symbol ":" denotes the doubled contracted product between two tensors. The hydrostatic pressure σ_{hyd} is defined as:

$$\sigma_{hyd} = -\frac{I_1}{3} \quad (5)$$

And the stress triaxiality η is written as:

$$\eta = -\frac{\sigma_{hyd}}{\sqrt{3J_2}} \quad (6)$$

The so-called Lode angle θ is related to the second and third invariant of the stress deviator by:

$$\theta = \frac{1}{3}\cos^{-1}\left(\frac{3\sqrt{3}}{2}\frac{J_3}{J_2^{\frac{3}{2}}}\right),\ 0 \le \theta \le \frac{\pi}{3} \quad (7)$$

The use of the dimensionless Lode parameter, $\bar{\theta}$, is more common in the literature, and is written as:

$$\bar{\theta} = 1 - \frac{6\theta}{\pi},\ -1 \le \bar{\theta} \le 1 \quad (8)$$

While the stress triaxiality and Lode parameter are in general independent variables, for plane-stress conditions, the following relation exists between them (Bai and Wierzbicki, 2008):

$$\cos\left[\frac{\pi}{2}(1-\bar{\theta})\right] = -\frac{27}{2}\eta\,(\eta^2 - \frac{1}{3}) \quad (9)$$

Using the stress triaxiality and Lode parameter, all forms of loading conditions can be distinguished. For instance, a shear state is characterized by the triaxiality and Lode parameter both equal to zero, uniaxial tension is characterized by stress triaxiality of 1/3 and Lode parameter of unity, plane-strain tension state has a triaxiality of $1/\sqrt{3}$ and Lode parameter of zero, and equi-biaxial tension is characterized by a triaxiality of 2/3 and Lode parameter of -1.

It should be noted that the use of the stress triaxiality and Lode parameter are convenient but has some important limitations. By definition, these measures are invariant and thus cannot account for anisotropy. The failure strains in the rolling and transverse directions of a material from a tensile test might be different but they will have the same stress triaxiality since the principal directions are not considered. Additional calibration parameters have been added into phenomenological fracture surfaces to account for anisotropy (*e.g.* Luo *et al*., 2012; Jia and Bai, 2016; Lou and Yoon, 2017) to generalize the failure *locus*. The appropriateness of using invariant to describe the stress state of anisotropic materials remains an open question. Furthermore, as discussed by Butcher and Abedini (2017), the stress triaxiality cannot differentiate between coaxial and non-coaxial stress states such as in pure and simple shear deformation. The stress triaxiality is zero for both of these shear loading cases, but the plastic work rates are different. Therefore, the work-conjugate equivalent strain will be different for the same level of major strain as the principal stress and the principal strain directions do not remain aligned in simple shear.

3.2. Proportional fracture characterization tests

A typical fracture testing program for sheet materials includes the main stress states of shear, uniaxial tension, plane-strain tension, and equi-biaxial tension under proportional conditions. Within this context, a proportional loading condition is defined when the principal stress and strain directions are coaxial and the stress triaxiality and Lode parameter are constant from initial deformation up to fracture. However, as schematically shown in Figure 4 for a typical tensile specimen, this is not the case when the characterization test leads to plastic instabilities, changing the loading conditions from their initial stress triaxialities and Lode parameters. For test geometries based upon in-plane tensile stretching, proportional loading ceases at the onset of

strain localization so it is important to select fracture tests that minimize necking and non-linear effects such as choosing a tight radius bend test for plane strain where necking is mitigated rather than a plane strain notch test. Recognizing that perfectly proportional tests across all stress states of interest is generally not possible from an experimental perspective, the present paper will define the selected fracture tests as "proportional" to differentiate from the non-proportional tests where the stress states are deliberately varied as described in Section 3.3.

Assessing the degree to which the "proportional tests" described in this section are not proportional is important since the deviation of the stress state generally coincides with the stress state becoming triaxial and no longer plane-stress. This deviation of the stress state is most apparent when using uniaxial tensile or notched tensile tests where the onset of necking occurs at comparatively low strains relative to the fracture strains. For the uniaxial test, the strain measurements of the surface will show a transition from uniaxial tension towards plane-strain but at the center of the specimen within the neck where failure initiates, the stress state is strongly triaxial. One could argue that such tests are neither plane-stress nor proportional and FE simulations with solid element are used in the literature to extract the stress state history (*e.g.* Dunand and Mohr, 2010; Anderson *et al.*, 2014) where the stress triaxiality is generally averaged for these tests (*e.g.* Bao and Wierzbicki, 2004).

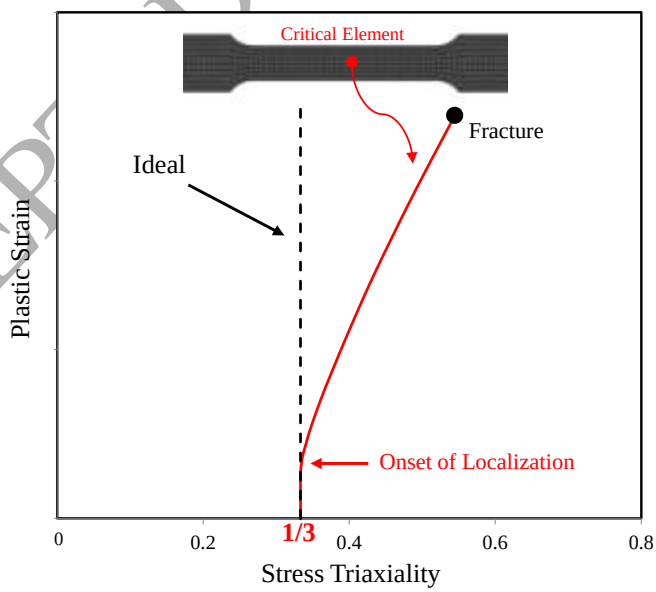

Figure 4 – Schematic of stress state deviations from the initial triaxiality for a tensile dogbone specimen.

The different types of specimen geometries used in the present paper for fracture characterization of ZEK100-O under proportional conditions are shown in Figure 5. The shear specimen depicted in Figure 5(a) was adopted from Peirs *et al.* (2012), and recently Abedini *et al.* (2015, 2017b) compared this specimen with the butterfly shear specimen of Dunand and Mohr (2011) (see Figure 5d) for different sheet materials and it was reported that both specimens performed well for fracture characterization of materials under a shear state while the shear specimen of Peirs *et al.* (2012) (Figure 5a) is marginally superior since it does not need through-thickness machining that may lead to surface micro-cracks. Moreover, this specimen can be loaded with conventional uniaxial frames as opposed to the butterfly specimen that requires a custom-made testing apparatus. Note that although the butterfly specimen will not be used in the present study for fracture characterization under the shear state, it will be utilized by taking advantage of its wide gauge width to impose a plane-strain tension condition as explained below. The shear tests with the specimen shown in Figure 5(a) were performed in the three directions of 0° (RD), 45°, and 135° with respect to the rolling direction. Note that in the shear state, the principal stress and strain directions are initially aligned at ± 45° to the applied loading direction. For instance, a shear test in the RD direction leads to the principal components in the ± 45° orientations. More information regarding shear tests for anisotropic and asymmetric materials and the choice of the test orientations can be found in Abedini *et al.* (2017a).

Typically, uniaxial tensile tests are performed with dogbone specimens; however, necking at low deformation levels limits their utility for studying large strains and for fracture characterization. Compared to regular dogbone specimens, the hole tension specimen shown in Figure 5(b) can delay the onset of necking and is a more representative test for fracture behaviour of materials under a uniaxial tension condition (Dunand and Mohr, 2010; Luo *et al.*, 2012; Kofiani *et al.*, 2013; Roth and Mohr, 2016; Pathak *et al*., 2017). Therefore, in the present study, the fracture response of the material under uniaxial tension is determined using the hole tension specimen shown in Figure 5(b). In addition, classical notch tensile tests provide means to control the stress triaxiality in tensile specimens and are commonly used in the literature (*e.g.* Dunand and Mohr, 2010; Lou and Yoon, 2017). It was mentioned earlier that these tests lead to early localization that makes interpretation of their results difficult; nevertheless, it is of interest in the present paper to perform these tests for the magnesium alloy, thus the notch specimen depicted in Figure 5(c) was utilized to obtain the response of the material with surface strain

paths lying between uniaxial and plane-strain tension. The hole tension and notch tension tests were conducted in three orientations corresponding to the RD, DD, and TD.

In addition, the plane-strain tension condition is a critical state for formability and fracture characterization of sheet metals that corresponds to the lowest ductility under plane-stress states (Mahmudi, 2009). Therefore, three different types of plane-strain tests were considered in the present study, namely, plane-strain butterfly test, hemispherical dome test, and v-bend test shown in Figures 5(d), (e), and (f), respectively. The v-bend tests were performed with the major axis of strain along either the RD, DD, or TD, while the plane-strain butterfly and dome tests were loaded along the RD and TD directions. All these specimens possess wide gauge widths that facilitate achieving a plane-strain condition with zero minor strain at the center of the gauge area. The plane-strain test results are compared and discussed in detail in Section 4.1.1. Finally, testing under the equi-biaxial tension state was conducted using a Nakazima hemispherical dome test with 200 mm $\times$ 200 mm blanks depicted in Figure 5(f).

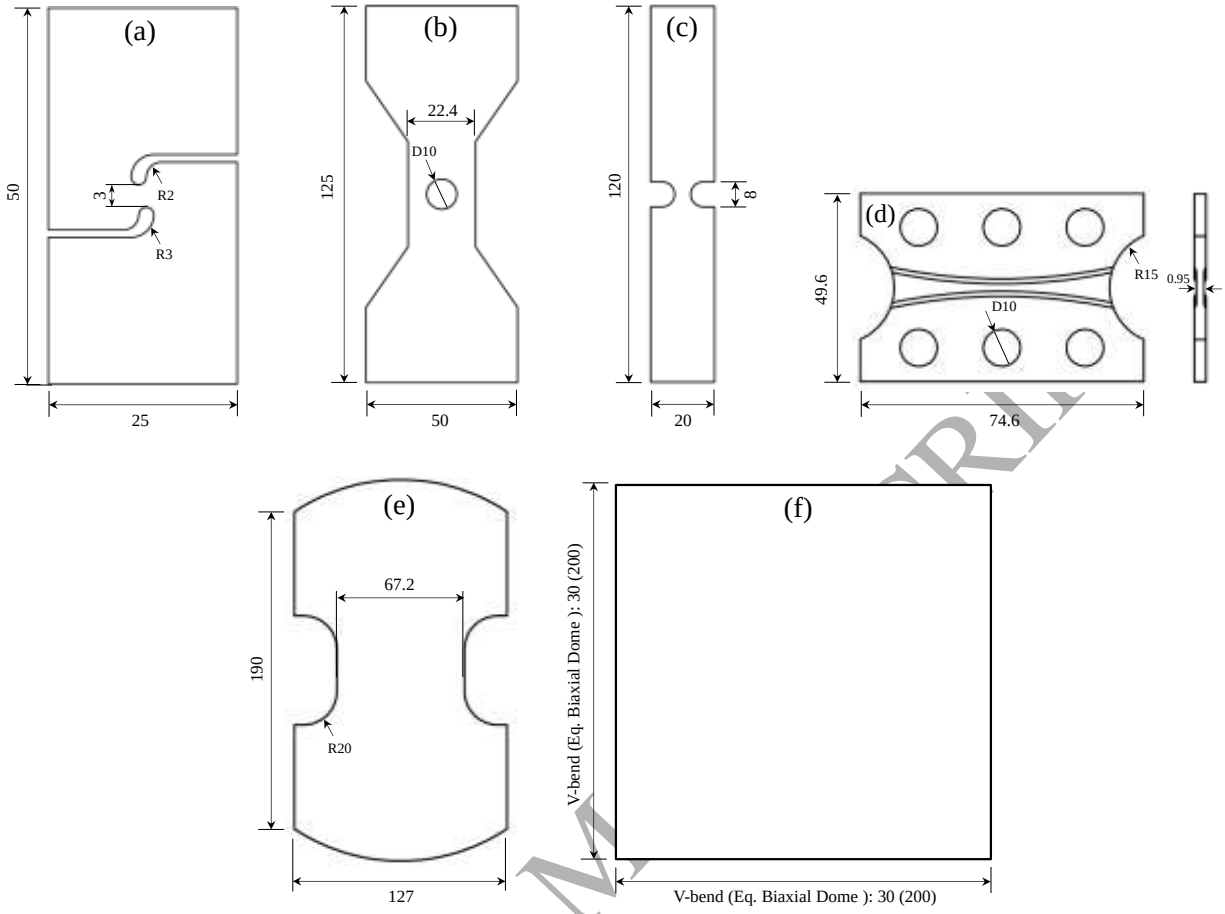

Figure 5 – Specimen geometries of (a) shear (Peirs *et al*., 2012), (b) hole tension, (c) notch tension, (d) butterfly (Mohr and Henn, 2007; Dunand and Mohr, 2011), (e) plane-strain dome, and (f) equi-biaxial dome and v-bend tests. All dimensions are in millimetres. For the in-plane tests (samples a-d) the load is applied in the vertical direction.

The tests described above were performed with different types of equipment. The shear, hole tension, and notch tension tests were performed using an MTS Criterion Model 45 servo-electric apparatus. The plane-strain butterfly test was performed with a displacement-controlled butterfly test frame in Figure 6(a) (see also Anderson *et al.*, 2017), and the plane-strain and equi-biaxial Nakazima dome tests were conducted with an MTS formability press with tooling shown in Figure 6(b) that conforms to the ISO12004-2 standard. Furthermore, the v-bend tests were done with a novel inverted v-bend test frame shown in Figure 6(c) that allows for direct strain measurements (Cheong *et al.*, 2017). The v-bend tests were performed according to the VDA 238-100 specifications utilizing a knife with a tip radius of 0.4 mm and a spacing between roller

supports of twice the sheet thickness of 1.55 mm. Note that in all the tests where tooling contact is required to impose deformation (dome and v-bend tests) Teflon® film lubricated with Vaseline® were used to reduce the influence of friction.

It is worth mentioning that fracture characterization of sheet materials under compressive loading is extremely difficult because of complexities in compression testing due to occurrence of buckling. Therefore, in the present study, the fracture response of the material was only characterized in stress states ranging from shear to biaxial stretching.

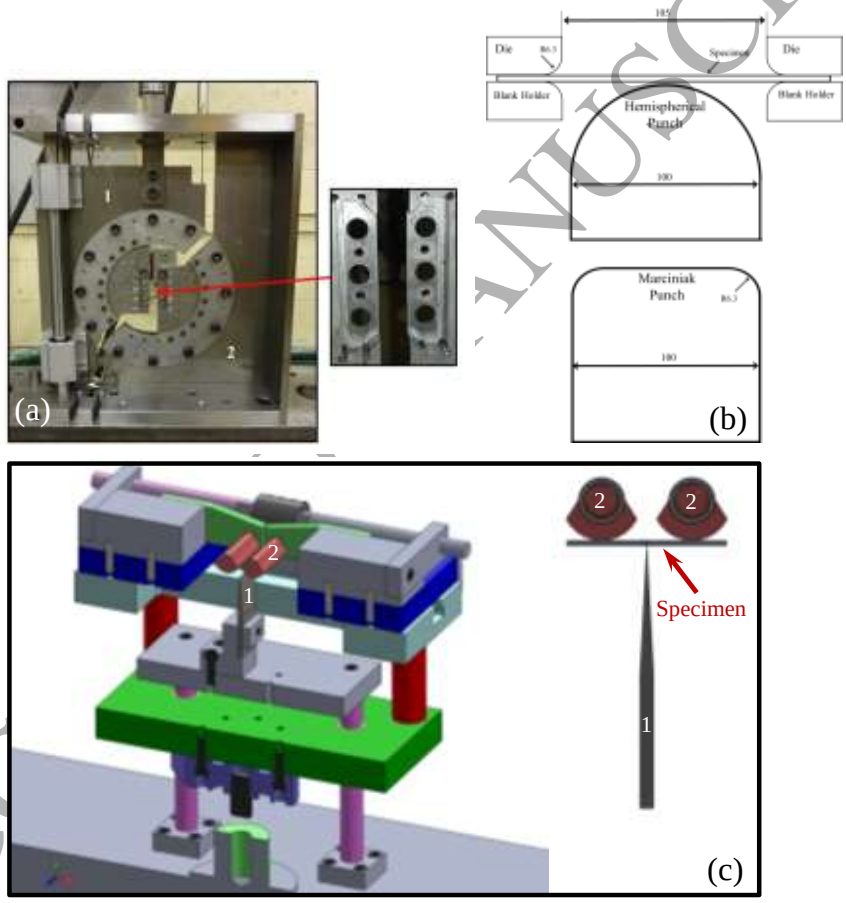

Figure 6 - Equipment used to perform experiments: (a) butterfly apparatus where labels (1) and (2) refer to the moveable and fixed parts, respectively. When the grips are rotated by 90°, plane-strain tension state is achieved, (b) dome test tooling, and (c) v-bend tester where labels (1) and (2) show the knife and rollers, respectively. All dimensions are in millimetres.

3.3. Non-proportional fracture characterization tests

To study the influence of non-proportional loading on fracture response of the material, two-stage tests were performed to induce significant changes in the stress state. For the first stage of the loading (pre-straining), two types of specimens were used: a scaled-up JIS tensile specimen shown in Figure 7(a) and an equi-biaxial Marciniak specimen shown in Figure 7(b). As a standard practice, the Marciniak test employs a carrier blank with a central hole in order to eliminate friction between the flat punch (see Figure 6b) and the centre of the blank. In the present study, AA5182-O carrier blanks with a central hole diameter of 50.8 mm were utilized. The uniaxial tensile test was performed in the rolling direction of the sheet using the MTS tensile frame. The first stages of deformation with uniaxial and equi-biaxial tension states were stopped at a plastic work level of 22.46 MJ/m^3. This deformation level was chosen since it corresponds to the onset of necking in the uniaxial tension test in the RD, thus the two first stages of deformation were interrupted at the same plastic work level. This plastic work level corresponds to von Mises equivalent strains of approximately 0.09 and 0.10 in the uniaxial and equi-biaxial tension tests, respectively (Figure 8). The tensile tests were carefully interrupted at the prescribed deformation level and no indication of necking or localized deformation was observed on the deformed specimens based on visual inspection and DIC measurements (see Figure 9).

It should be mentioned that the biaxial stresses cannot be extracted from the Marciniak tests thus prior to these tests a primary characterization test was performed with through-thickness compression of stacked sheet specimens (Abedini *et al*. 2017a) to obtain the approximate stress-strain response of the material in equi-biaxial tension (Figure 8). The equi-biaxial tension and through-thickness compression tests are considered to be equivalent stress states for plastic characterization of materials since they possess the same stress deviator (Steglich *et al*., 2014). Subsequently, the punch movement in the Marciniak tests was terminated at the punch height associated with the von Mises equivalent strain of 0.10 determined with the aid of the DIC measurements. Note that due to the complex anisotropy of the magnesium alloy, the plastic work measure was selected to stop the pre-straining deformation. The definition of the plastic work (Eq. 1) is independent of adopted constitutive plasticity models and can be used to interrupt the first stages of loading at an equivalent level of plastic deformation.

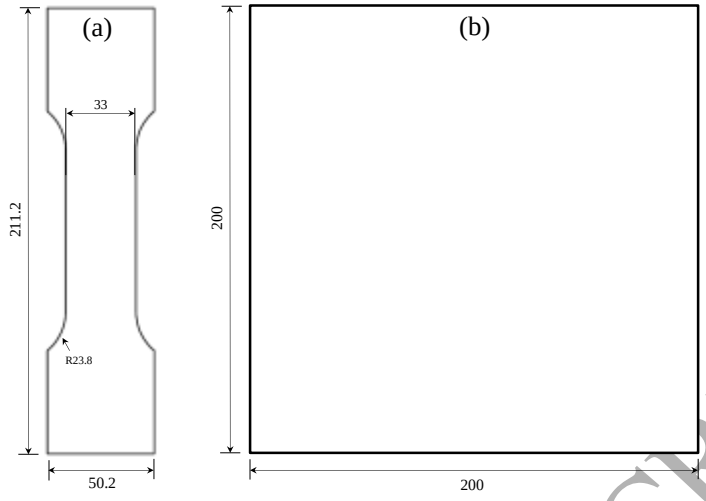

Figure 7 – Specimen geometries of (a) scaled JIS and (b) Marciniak tests. All dimensions are in millimetres.

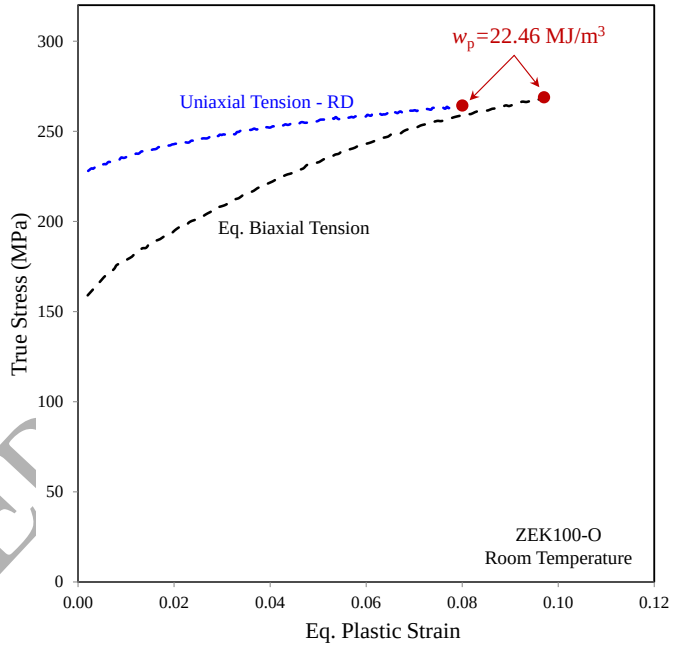

Figure 8 – Uniaxial and equi-biaxial tensile response of ZEK100-O at room temperature under a quasi-static strain rate of 0.001 s^{-1}. For the non-proportional tests, the first stages of deformation were stopped at the plastic work level of 22.46 MJ/m^3. Note that the equi-biaxial data is from through-thickness compression tests in Abedini *et al.* (2017a).

Subsequently, simple shear and v-bend specimens shown in Figures 5(a) and 5(f), respectively, were extracted from the pre-strained specimens to apply the second stages of loading, as presented in Table 1. As shown in Figure 9, the shear and v-bend specimens were extracted from the uniformly deformed regions of the Marciniak and tensile specimens. Also note that this region of the Marciniak specimen is in the cut-out area where there is no frictional contact and deformation is plane-stress. As mentioned earlier, the tests were interrupted before the onset of plastic localization; therefore; surface strain measurements are representative of deformation of the sheet since there are no through-thickness strain gradients. The two-stage nature of stress histories in the non-proportional tests is also shown schematically along with theoretical stress triaxialities in Figure 10 where it can be seen that the initial stress states are abruptly switched to plane-strain tension and shear states. The v-bend specimens were fabricated in the RD and TD directions while the shear samples were extracted in the RD direction only. These specimens were subsequently tested up to fracture using the same procedure explained for proportional tests. Note that all of the specimens used in the present study were fabricated by CNC machining.

Table 1 – Description of stress state change in non-proportional tests.

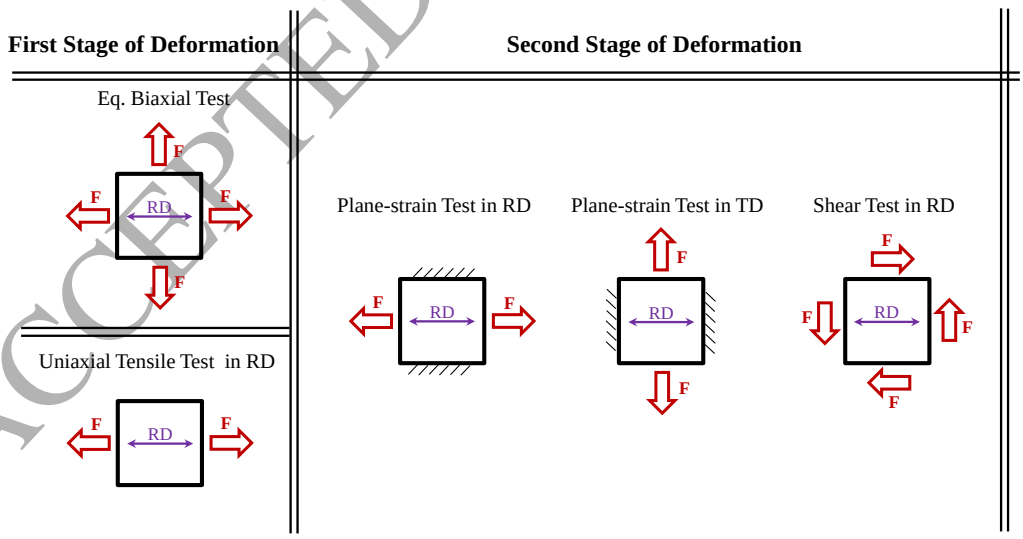

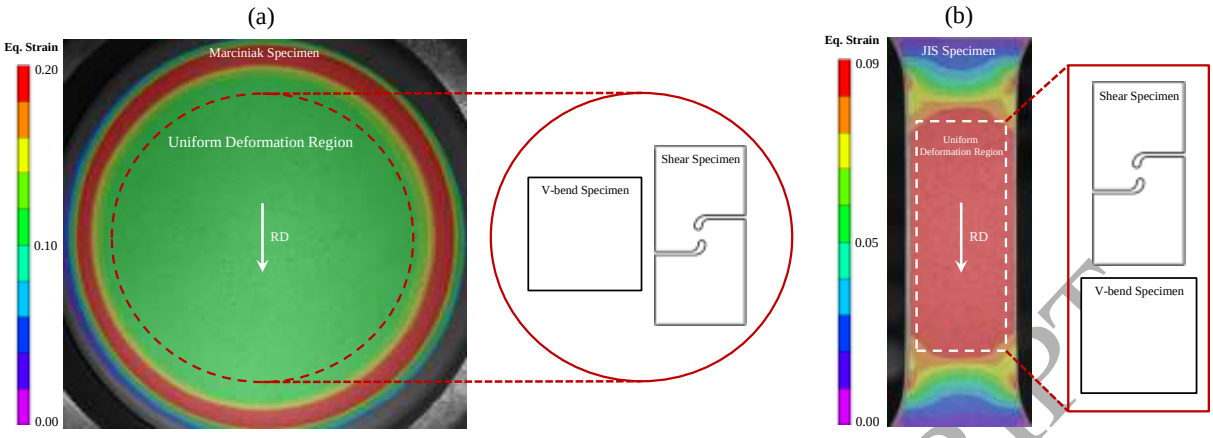

Figure 9 – Specimens extracted at the end of the first stages of the non-proportional tests from the uniformly deformed regions of (a) Marciniak and (b) JIS tensile specimens. The measured DIC contours of equivalent strain are also depicted.

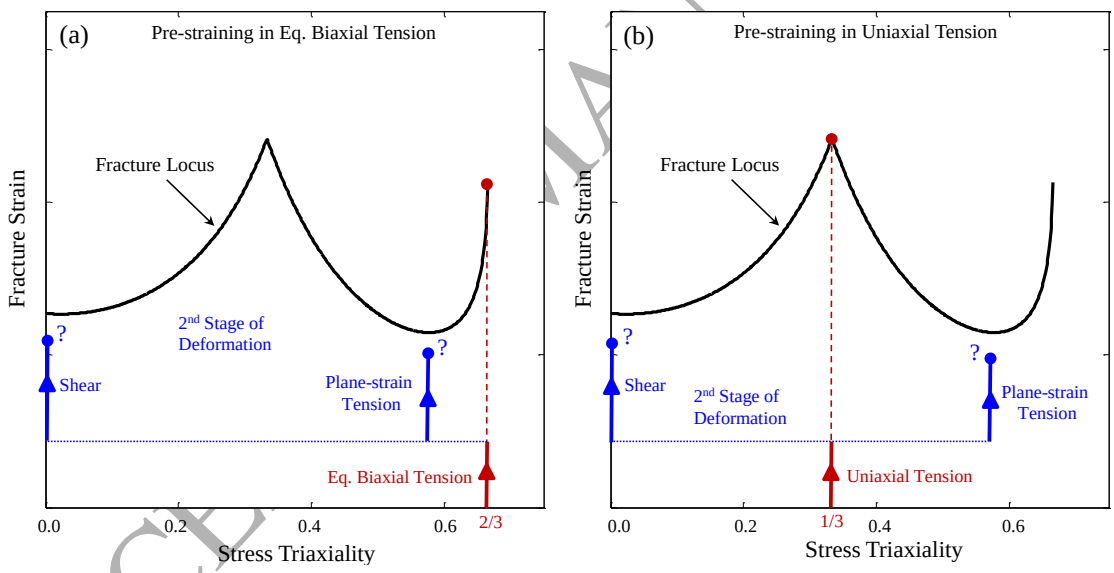

Figure 10 – Schematic illustration of first and second stages of deformation shown on a fracture *locus* for (a) equi-biaxial and (b) uniaxial tension pre-straining. Note that the initial uniaxial pre-straining was performed in the RD only. Also subsequent tests for the second stages of deformation were performed in the RD for the shear tests and in the RD and TD for the v-bend tests. Question marks show the unknown fracture strains in non-proportional tests.

3.4. Strain measurements

The experiments described above were recorded using digital cameras to obtain full-field logarithmic strain measurements using digital image correlation (DIC) techniques. The commercial VIC3D DIC software from Correlated Solutions, Inc. was used for the DIC analysis. The images were recorded using two Point Grey 4.1 MP cameras for stereoscopic DIC measurements. Depending upon the size of the specimens, different types of lenses were utilized, resulting in various image resolutions; however, a virtual strain gauge length (VSGL = resolution [mm/pixel] × step size [pixel] × filter size) of 0.3 mm was used for all the tests. It was shown by Rahmaan *et al.* (2017) that a VSGL of 0.3 mm is sufficiently small for fracture characterization of the shear specimen which is the smallest specimen used in this study. For consistency, the DIC analyses of rest of the (larger) specimens were also performed with the same VSGL size. More information regarding the VSGL size and its influence on the DIC strain measurements can be found in Reu (2015) and Rahmaan *et al.* (2017). The DIC images in each experiment were recorded with a prescribed frequency to provide at least 300 images from the initial deformation up to fracture. The DIC parameters associated with each test are presented in Table 2.

Table 2 – DIC parameters for full-field stereoscopic strain measurements.

Test	Image Resolution (mm/pixel)	Step Size (pixel)	Filter Size	VSGL (mm)
Shear	0.023	2	7	~0.3
Hole Tension	0.021	2	7	~0.3
Scaled JIS	0.060	1	5	~0.3
Notch Tension	0.021	2	7	~0.3
V-bend	0.021	2	7	~0.3
Plane-strain Butterfly	0.039	1	7	~0.3
Plane-strain Dome	0.056	1	5	~0.3
Eq. Biaxial Dome	0.056	1	5	~0.3
Eq. Biaxial Marciniak	0.056	1	5	~0.3

When it comes to reporting fracture strains, it is common in the literature to provide equivalent strain measurements. However, equivalent strain measures are a function of the adopted constitutive plasticity model (Butcher and Abedini, 2017), so they require knowledge of

appropriate yield functions and their coefficients. Given the complex evolving anisotropy of ZEK100-O, this is a challenging task and will not be considered in the present study. Instead, the von Mises equivalent fracture strains are reported along with the components of the strain tensor so that the interested reader can re-cast them in terms of the adopted constitutive models. The von Mises equivalent strain rate, $\dot{\varepsilon}_{VM}$, is written as:

$$\dot{\varepsilon}_{VM} = \frac{2}{\sqrt{3}} \sqrt{\dot{\varepsilon}_1^2 + \dot{\varepsilon}_2^2 + \dot{\varepsilon}_1 \dot{\varepsilon}_2} \tag{10}$$

where $\dot{\varepsilon}_1$ and $\dot{\varepsilon}_2$ are the measured principal strain rate components. The von Mises equivalent strain, ε_{VM}, is calculated by integrating the equivalent strain rate using the measured DIC time increments:

$$\varepsilon_{VM} = \int \dot{\varepsilon}_{VM} \, dt \tag{11}$$

Note that as discussed in Butcher and Abedini (2017), Eq. (10) is strictly valid for coaxial loading conditions. Non-coaxiality may develop specifically for shear tests since the stress state is close to the simple shear definition in which the principal stress and strain components rotate during deformation with different rates; however, for the current magnesium alloy with relatively low ductility (major principal strain at fracture of about 0.2 under shear state) the difference between the coaxial formulation of Eq. (10) and the work-conjugate definition remain negligibly small and the principal stress and strain directions remain closely coaxial. Therefore, Eq. (10) was used to determine the equivalent fracture strains in shear loading.

All of the tests described above were conducted at room temperature, under a quasi-static von Mises equivalent strain rate of approximately 0.001 s^{-1}. To assess the repeatability of the results, at least four specimens per loading condition and orientation were tested which resulted in approximately 100 tests in total to reveal the constitutive fracture behaviour of ZEK100-O magnesium alloy under different proportional and non-proportional stress states.

3.4.1 Fracture initiation location

Figure 11 shows the DIC images at the time of appearance of the first detectable discontinuity on the specimen surface which is defined as the onset of fracture. Consequently, DIC measurements were performed up to the last image before the onset of fracture. The fracture strains were reported by averaging strains of all points within a circle inspector with a diameter of 0.3 mm at the fracture initiation locations. This circle size was chosen for consistency with the VSGL size. The locations where fracture initiates were identifiable for all specimens except for the shear and notch specimens. However, it was shown in Peirs *et al.* (2012) and Abedini *et al.* (2015) that fracture initiated from the center of the shear specimen for Ti6Al4V and DP600 sheets, respectively. For the current shear and notch tension specimens, the fracture strains were measured at the center of the gauge area where the highest strains occur. It is worth mentioning that, recently, Rahmaan *et al*. (2017) showed that using microscopic strain measurements based upon the grain rotation within the shear band can resolve even larger shear fracture stains than reported by the DIC, specifically for elevated strain rates. This difference was due to the collapse of the shear band into a severe micro shear-band where failure initiates and the gauge length imposed by the VSGL inherent in the DIC calculations. Thus, the shear failure strain obtained using the DIC in the present work must be recognized to be very sensitive to the length scale.

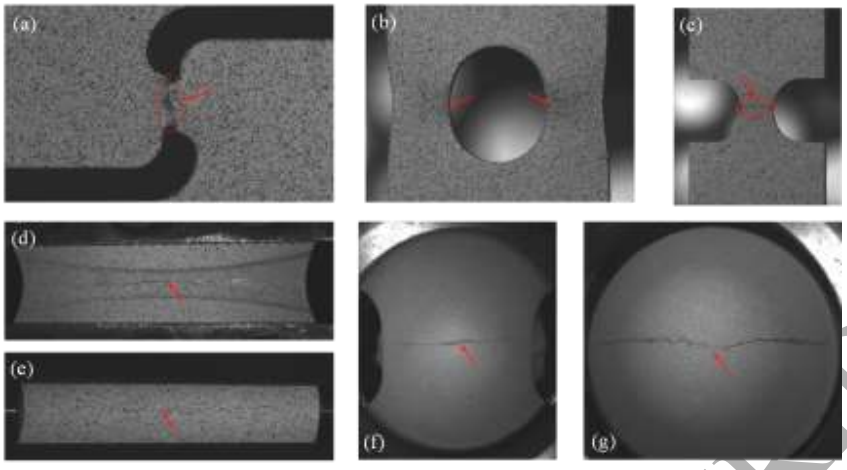

Figure 11 – The DIC images captured at the time of first appearance of visible crack on the surface of (a) shear, (b) hole tension, (c) notch tension, (d) plane-strain butterfly, (e) v-bend, (f) plane-strain dome, and (g) equi-biaxial dome specimens. Images (a-f) correspond to tests in the RD. Arrows show the crack locations.

Concerning the hole tension specimen, Pathak *et al.* (2017) showed that fracture strains obtained from this specimen are comparable to that of a hole expansion test (an alternate test for uniaxial tension fracture characterization) for CP800 and DP780 steels. It should be noted that fracture in the hole tension specimen may initiate away from the edge where the stress state is not uniaxial tension (Anderson *et al.*, 2017). The hole tension specimen geometry used in the present study is the same as used by Pathak *et al*. (2017) for a DP780 sheet with the same nominal thickness as the ZEK100-O (1.55 mm). It is emphasized that fracture initiated from the edges of the hole in the ZEK100-O tests. A more detailed study on the geometry of the hole tension specimen can also be found in Roth and Mohr (2016).

3.5. Phenomenological fracture model

Numerous uncoupled phenomenological fracture models have been developed in the literature which ignore the effects of damage on plastic behaviour of materials prior to fracture; therefore, one can utilize any standard metal plasticity model along with a separate phenomenological fracture model (*e.g.* Oyane *et al.*, 1980; Clift *et al.*, 1990; Bai and Wierzbicki, 2008; 2010; Lou and Huh, 2013; Mohr and Marcadet, 2015). The Bai-Wierzbicki model (Bai and Wierzbicki,

2010) has received considerable attention in the literature and it has been reported that the model is capable of predicting fracture with a good accuracy for various alloys (*e.g.* Malcher *et al.*, 2012; Gurben *et al.*, 2012; Cao *et al.* 2013; Lian *et al.* 2013; Kofiani *et al.*, 2013; Rousselier and Luo, 2014; Wang *et al.*, 2015). Therefore, this model was adopted in the present study to construct the fracture *locus* for ZEK100-O. The Mohr-Coulomb criterion postulates that fracture takes place in a body on a plane on which the combination of the normal and shear stresses reaches a critical value. Bai and Wierzbicki (2010) adopted the Mohr-Coulomb model and transformed it into a stress triaxiality and Lode parameter dependent formulation. They showed that the equivalent strain at fracture, ε^f, in the Mohr-Coulomb criterion can be written in the space of the stress triaxiality and Lode parameter. This formulation has been re-cast into the form of:

$$\varepsilon^f = \left\{ c_1 \left[\sqrt{\frac{1+c_2^2}{3}} \cos\left(\frac{\bar{\theta}\pi}{6} \right) + c_2 \left(\eta + \frac{1}{3}\left(\frac{\bar{\theta}\pi}{6} \right) \right) \right] \right\}^{c_3} \tag{12}$$

where the parameters $c_{1\text{-}3}$ are obtained from experimental tests. The equivalent failure strain can be calibrated from the experiments and is implicitly coupled to the constitutive model which is used to convert the equivalent failure strain to a stress depending on the hardening function and stress state. As explained in Section 3.1, for the case of plane-stress conditions, stress triaxiality and Lode parameter are not independent (Eq. 9); therefore, Eq. (12) reduces to a single variable function.

Note that the phenomenological fracture model in Eq. (12) has been proposed for isotropic materials; however, ZEK100-O is anisotropic, thus the model will be calibrated to individual material orientations to evaluate the degree of direction-dependency in the fracture behaviour of the material. It was assumed that the stress triaxialities in each test are constant and are equal to the theoretical values given in section 3.1. Experimentally, strain paths can be converted to the stress triaxiality but this requires knowledge of the plasticity model and for magnesium it is extremely complex with evolving anisotropy. To enable the development and assessment of an analytical damage model, these constant stress states are required to side-step employing a finite element model. The non-proportional tests have been carefully designed to ensure homogeneous plane-stress deformation to support the analytical framework. Therefore, the results of the

phenomenological fracture surface can provide a simple representation of stress state dependency and anisotropy of ZEK100-O under different orientations.

4. Results and discussion

4.1. Proportional tests

Figure 12 displays the DIC strain contours of major and minor strains corresponding to the last image before the onset of fracture, while their associated load-displacement responses are shown in Figure 13. For brevity, only the results of the tests in the RD are shown in Figure 12 while the strain paths of tests with different orientations are shown in Figure 14 in terms of major *versus* minor strains. Note that for the plane-strain cases, only the results of the v-bend tests are shown in Figure 14 since the response of the material exhibits an almost perfectly plane-strain condition with zero minor strains. Also note that all of the plane-strain tests are discussed and compared in detail in Section 4.1.1. Components of the fracture strains are presented in Table 3 along with the von Mises equivalent fracture strains. As mentioned earlier, at least four tests were performed for each stress state and orientation and the standard deviations (SD) are included in Table 3.

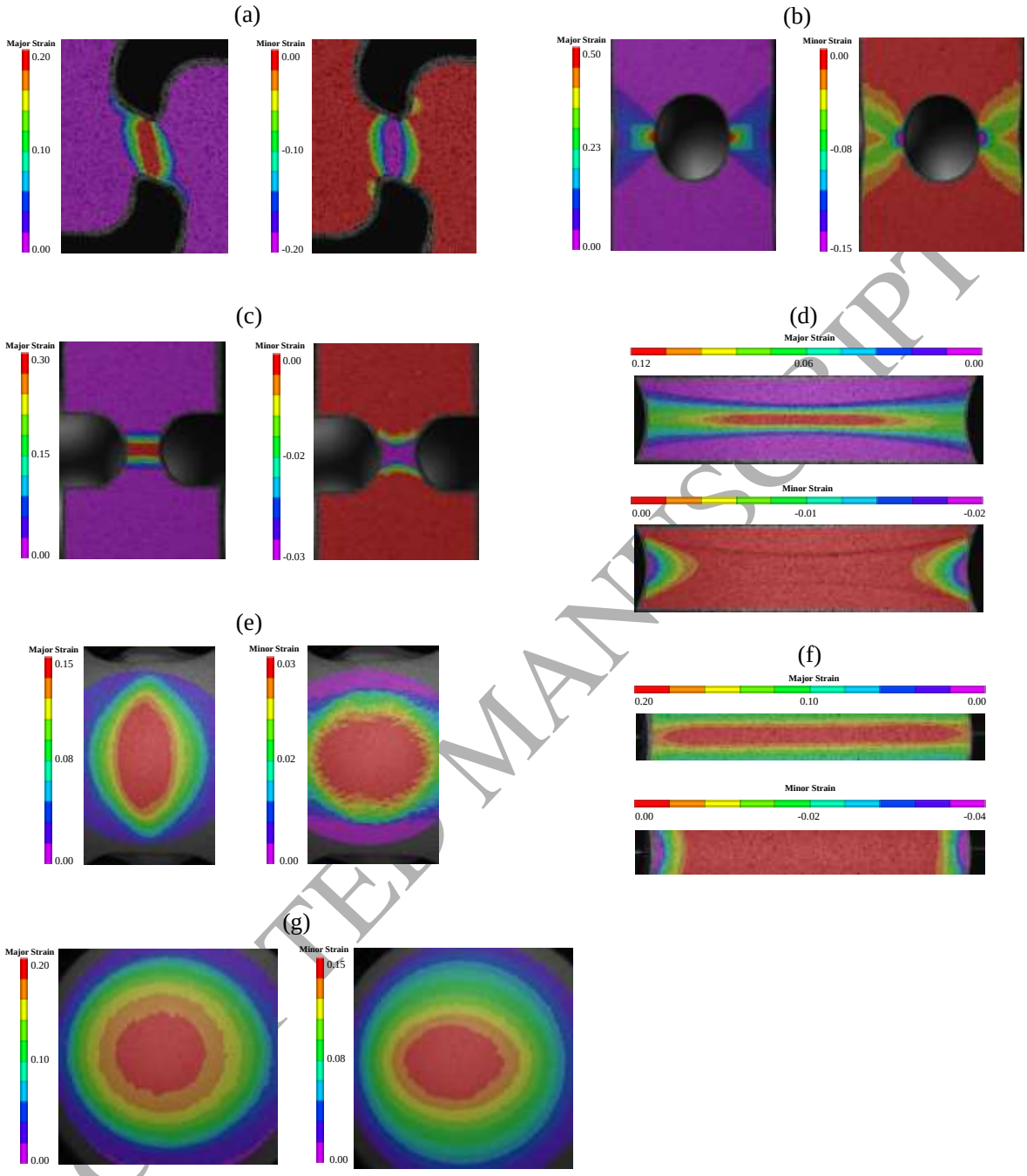

Figure 12 – Contours of DIC strains obtained at the last image before the appearance of visible crack on the surface of specimens of (a) shear, (b) hole tension, (c) notch tension, (d) plane-strain butterfly, (e) plane-strain dome, (f) v-bend, and (g) equi-biaxial dome specimens. Figures (a-f) correspond to tests in the rolling direction.

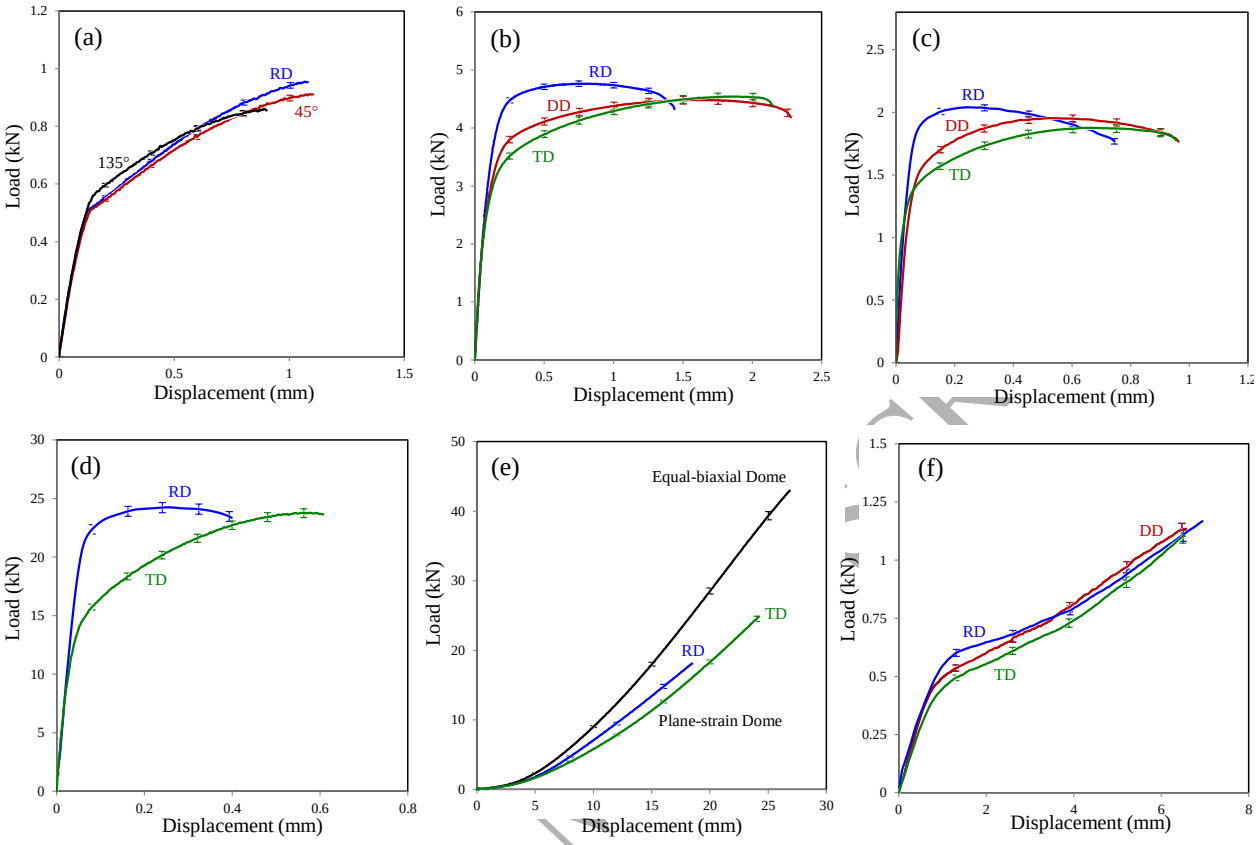

Figure 13 – Load-displacement responses of different specimens of (a) shear, (b) hole tension, (c) notch tension, (d) plane-strain butterfly, (e) Nakaziam dome, and (f) v-bend tests. Note that the sigmoidal shape of the v-bend test is due to compressive components in the inner layers of the bend. In-plane compressive stresses are known to activate twinning mechanisms to accommodate plastic straining.

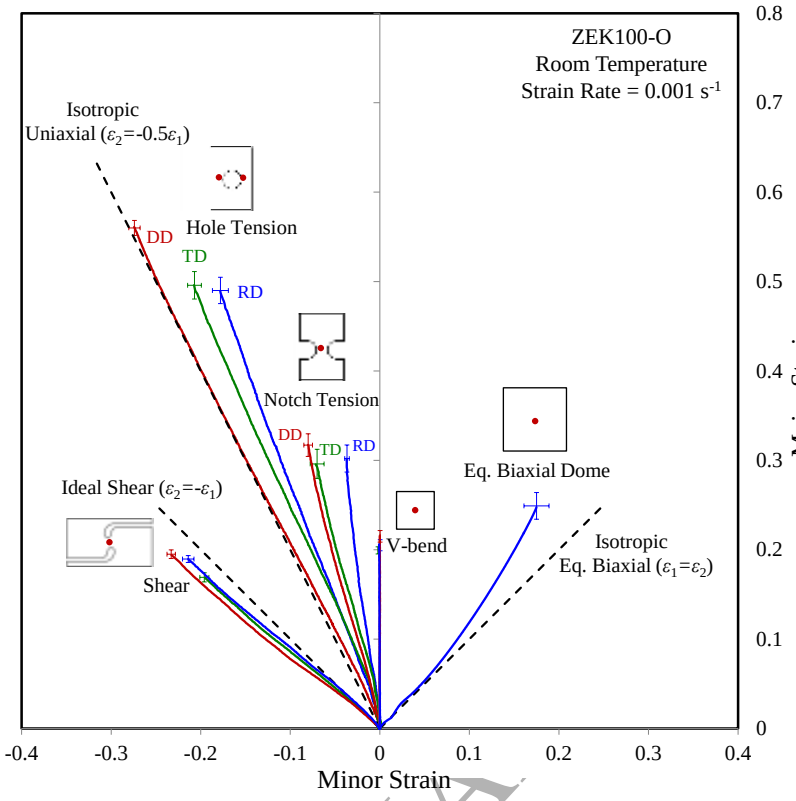

Figure 14 – Strain paths to fracture for different proportional tests. The ideal strain paths for proportional loading of isotropic materials are also shown for comparison.

Table 3 – Fracture strains obtained from characterizing proportional tests performed in different orientations. SD stands for standard deviations. Note that due to the nearly zero minor strains in the plane-strain v-bend and butterfly tests, zero values appear for minor strains and their SD when these are reported with two decimal places.

Tests	Orientation	ε_1 (SD)	ε_2 (SD)	von Mises Eq. Strain (SD)
Shear	RD	0.19 (0.01)	-0.22 (0.01)	0.24 (0.01)
	45°	0.20 (0.01)	-0.24 (0.01)	0.25 (0.01)
	135°	0.17 (0.01)	-0.20 (0.01)	0.21 (0.01)
Hole Tension	RD	0.48 (0.01)	-0.17 (0.01)	0.48 (0.01)
	DD	0.60 (0.01)	-0.28 (0.01)	0.60 (0.01)
	TD	0.50 (0.02)	-0.22 (0.01)	0.50 (0.02)
Notch Tension	RD	0.31 (0.03)	-0.04 (0.00)	0.34 (0.04)
	DD	0.34 (0.03)	-0.08 (0.01)	0.35 (0.03)
	TD	0.29 (0.03)	-0.07 (0.01)	0.31 (0.04)
V-bend	RD	0.20 (0.01)	0.00 (0.00)	0.23 (0.01)
	DD	0.21 (0.01)	0.00 (0.00)	0.25 (0.01)
	TD	0.20 (0.01)	0.00 (0.00)	0.23 (0.01)
Plane-strain Butterfly	RD	0.14 (0.02)	0.00 (0.00)	0.17 (0.02)
	TD	0.15 (0.01)	0.00 (0.00)	0.17 (0.01)
Plane-strain Dome	RD	0.20 (0.01)	0.03 (0.00)	0.25 (0.01)
	TD	0.20 (0.01)	0.01 (0.00)	0.24 (0.01)
Eq. Biaxial Dome	-	0.25 (0.02)	0.18 (0.02)	0.43 (0.04)

It can be seen from Figure 14 that the material exhibits orientation-dependent strain paths and fracture behaviour. Anisotropy in the strain paths is more pronounced for the hole tension and notch tension tests. Furthermore, the equi-biaxial tension test shows a strain path which is initially close to equal principal strains while it deviates from this condition for larger deformation due to the onset of localization leading to fracture occurring in the RD direction.

Of particular interests are the strain paths corresponding to the shear tests that deviate from the ideal principal strain path of equal and opposite strains ($\frac{\varepsilon_2}{\varepsilon_1} = -1$). As discussed by Abedini *et al.* (2017c), this strain path for simple shear tests is a direct consequence of the kinematics of simple shear from the imposed deformation gradient and is thus independent of the material. The strain path for ZEK100-O initially follows the simple shear strain path near yielding but then deviates towards a more compressive strain path. Assuming volume conservation for

deformation of the magnesium alloy, the results of Figure 14 suggest that the thickness of an element subjected to shear state increases with deformation. The Swift phenomenon, defined as the occurrence of axial plastic deformation during monotonic free-end torsion of solid rods or tubes (Swift, 1947), might be responsible for this behaviour. Recently, Guo *et al.* (2013) related the Swift phenomenon to twinning mechanisms activated during plastic deformation of hcp alloys, a description which is in line with the twinning activities reported by Abedini *et al.* (2017a) for shear tests of ZEK100-O using electron backscattered diffraction (EBSD) analysis. It should be noted that this observation in the shear tests is not due to the selection of the shear geometry since ideal strain paths with equal and opposite principal strains have been previously reported for shear tests on different fcc and bcc materials with the same specimen geometry (Abedini *et al*., 2017b,c; Rahmaan *et al*., 2017).

The fracture strains depend on the imposed stress states and orientations. To visualize this better, the phenomenological fracture curve described in Section 3.5 was calibrated to the experimental data in three directions corresponding to the RD, DD, and TD, with the associated coefficients given in Table 4 and the results shown in Figure 15. Note that the notch tension tests were not considered for the calibration since these tests are known to exhibit a pronounced increase in the stress triaxiality from the onset of plastic deformation (Dunand and Mohr, 2010; Beese *et al.*, 2010). Furthermore, due to the significant strain localization, the stress state is no longer plane-stress with severe through-thickness stress gradients. Due to these reasons, the notch tensile tests were excluded from calibration of the phenomenological fracture curve.

When it comes to stress state dependency, it can be seen from Figure 15 that the plane-strain tension condition has the lowest fracture strain closely followed by the shear state while the material shows the highest ductility under the uniaxial tension condition for all orientations. In terms of anisotropy, it can be seen from Figure 15 that the DD direction possesses the highest ductility while the fracture strains in the RD and TD directions are comparable. Anisotropy in fracture is most significant under the uniaxial tension condition in which the DD direction displays approximately 20% higher ductility than the RD and TD directions while the plane-strain condition exhibits a negligible directional sensitivity. It should be mentioned that the equi-biaxial state is direction independent, in other words, all the directions on the plane of the sheet experience an equal magnitude of stress which is the underlying reason why all the fracture

curves converged at the equi-biaxial point in Figure 15, and the same fracture strain was used to calibrate the curves at this point. However, the material eventually fails from a limiting direction that was observed to be the RD for equi-biaxial dome tests on ZEK100-O.

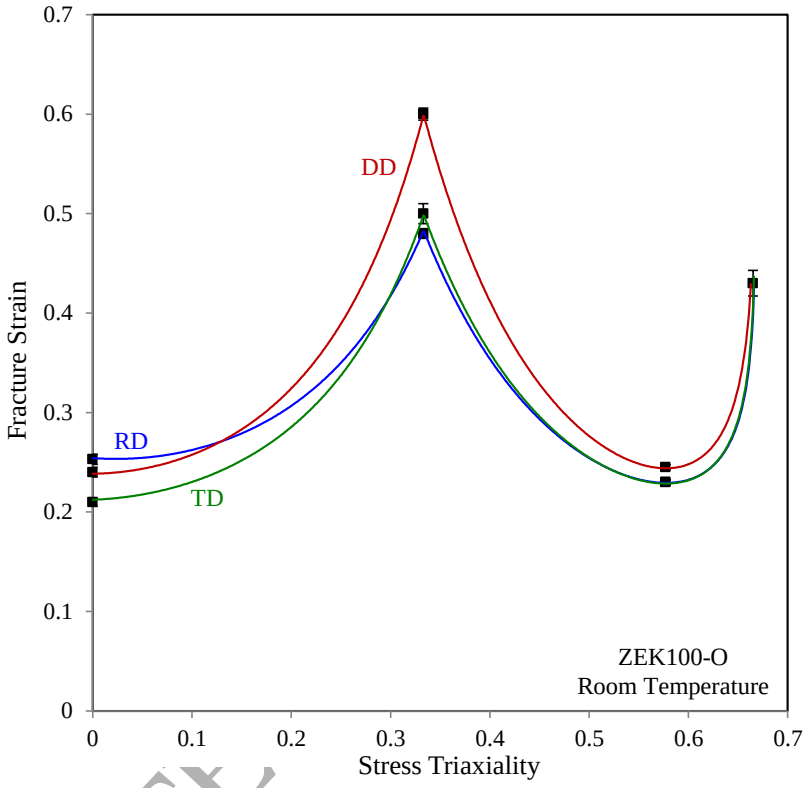

Figure 15 – Fracture *locus* under proportional conditions. Symbols show the average experimental data.

Table 4 – Coefficients of the phenomenological fracture model (Eq. 12).

Orientation	c_1	c_2	c_3
RD	0.8307	0.0547	-5.1814
DD	1.9767	-0.0040	-6.2539
TD	1.9541	-0.0160	-5.4289

It is important to note the general shape of the fracture *loci* in Figure 15 where the failure strain in shear is markedly lower than in uniaxial tension and is very similar to that of plane-strain tension. Whether the shear failure strains should be lower than uniaxial tensile loading is a current source of controversy in the literature and potentially might be related to the choice of the shear test specimen. For instance, Scales *et al*. (2016) conducted torsion tests on AA6061-T6 tubes and observed that the shear fracture strain of the material is significantly (about 300%) higher than that of reported by Beese *et al*. (2010) for AA6061-T6 sheets with an in-plane shear specimen. However, conducting torsion tests is not experimentally feasible for sheet metals. In-plane shear specimens are highly susceptible to fracture initiation from free boundaries where deformation is close to uniaxial states. In such cases, the strain at the center of the gauge area (shear zone) can only be considered as a lower-bound estimate of the fracture strain under the shear state. It should be mentioned that, for the magnesium alloy considered in the present study, Abedini *et al*. (2017b) conducted shear tests with the butterfly specimen where fracture was detected to clearly initiate from the center of the gauge section and not the specimen edges and the fracture strains were comparable to the values obtained with the shear specimen used in the present study. It is worth mentioning that, recently, Rahmaan *et al*. (2017) have shown that gauge lengths are critical for shear tests and that local shear strains measured microscopically near the fracture surface resolved from grain rotations can be much higher than the strains reported from DIC measurements that average the strains over a larger area.

4.1.1. Selection of appropriate test geometry for plane-strain tension

The plane-strain condition is critical for sheet metal forming operations since most materials exhibit their lowest ductility under this state of deformation. During an automotive crash event, structural components such as crush rails fold and tight-radius bends are commonly formed within which the state of stress is plane-strain tension at the outer radius of the bend. Due to the importance of this loading condition, this section is devoted to comparing the results of all the three plane-strain tension tests performed in the present study. Figure 16 shows the strain paths to fracture from the three tests, namely the plane-strain dome, butterfly, and v-bend, in the RD direction. It can be seen that all of the tests lead to strain paths close to the desired plane-strain condition with small minor strains. The strain path of the v-bend test lies almost perfectly on the

zero minor strain axis and the strain path of the plane-strain butterfly test is also close to the perfect condition. However, the plane-strain dome test shows some deviations from an ideal plane-strain path for small deformation which is due to biaxial bending associated with the dome radius (Hotz and Timm, 2008).

Furthermore, in terms of the fracture strains in Figure 16 and Table 3, it can be observed that the v-bend test results in higher fracture strains than the other two tests, specifically, the fracture strains are significantly higher than those of the plane-strain butterfly test. The reason for the generally higher fracture strains in the v-bend test can be correlated to the location where the maximum strain occurs in the specimen. As opposed to the plane-strain dome and butterfly specimens in which the maximum strains occur through the thickness on the mid-plane (Dunand and Mohr, 2010), the maximum strains in the v-bend test happen on the surface of the specimen with strong strain and stress gradients through the thickness. It is argued by Morales-Palma *et al*. (2013) that such gradients help with suppressing the onset of plastic localization in tight-radius bending resulting in a proportional test to fracture. Moreover, the DIC method is only capable of capturing strains on the surface; therefore, strains at the center of the butterfly and dome specimens at the time of fracture are expected to be closer to the fracture strain on the surface of the v-bend specimen. It should be noted that through-thickness strain gradients with maximum values on the mid-plane exist more or less for all of the tensile specimens used in this study so that the fracture strains on the surfaces are lower-bound estimates for the ductility of the material. This highlights the advantage of the v-bend test for fracture characterization of sheet under plane-strain conditions, with fracture strains that can be more representative of the failure strains observed in tight-radius bends in crashworthiness experiments of crush rails (Omer *et al*., 2017).

In addition, as discussed by Abedini *et al.* (2017b), using through-thickness machining for fabricating specimens, increases the likelihood of initiating fracture at a local discontinuity as a result of machining-induced defects. In general, specimens that do not require through-thickness machining are more suitable for fracture characterization. The butterfly specimen features a large through-thickness machined section that represents a potential reason for lower fracture strains compared to the other two specimens. Despite this drawback, it should be mentioned that the butterfly is a versatile specimen that can be used to characterize fracture over a range of stress

states (Mohr and Henn, 2007; Anderson *et al.*, 2017) although only the plane-strain state was utilized in the present study.

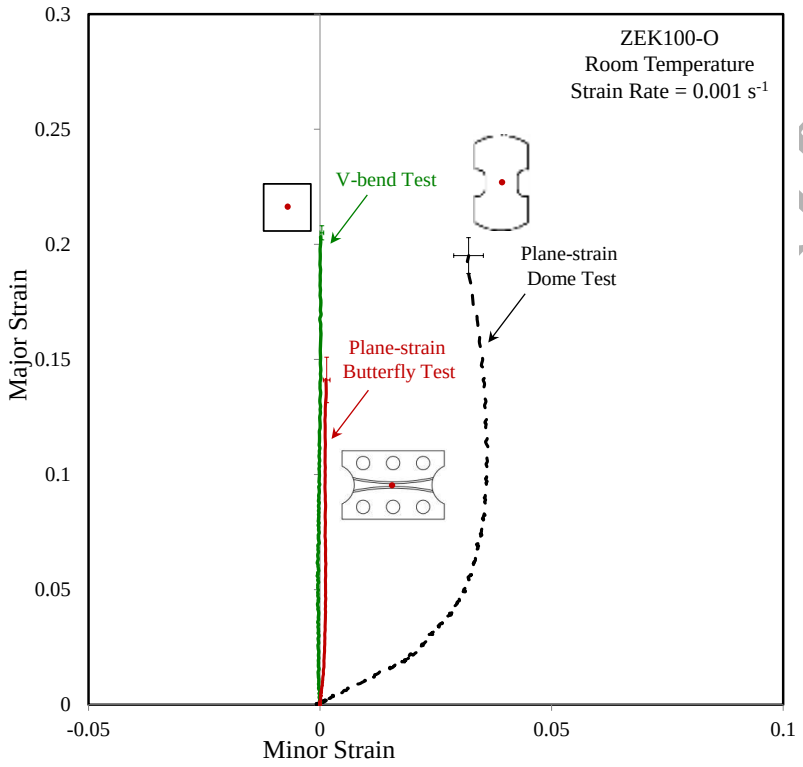

Figure 16 – Strain paths to fracture for different plane-strain tests. All the tests were performed in the RD.

4.2. Non-proportional tests

The load-displacement responses and the strains at the time of fracture for the non-proportional tests are given in Figure 17 and Table 5, respectively. Note that for the results presented in Figure 17 and Table 5, the pre-strained material was treated as a new material thus the deformation corresponds only to the second stages of the loading without considering the initial strains existing in the material from the first stages of the deformation. Based on this assumption, the fracture strains in the proportional and non-proportional tests are compared in Figure 18. It can be seen that the fracture strains under the shear state are not significantly influenced by pre-straining; however, the fracture strains for the plane-strain tension condition

are reduced by the pre-straining deformation. The decrease of the fracture strains in the plane-strain v-bend tests is similar for both orientations of the RD and TD. Furthermore, it can be seen from Figure 18 that the reductions in fracture strain in the plane-strain condition are more remarkable after biaxial pre-straining.

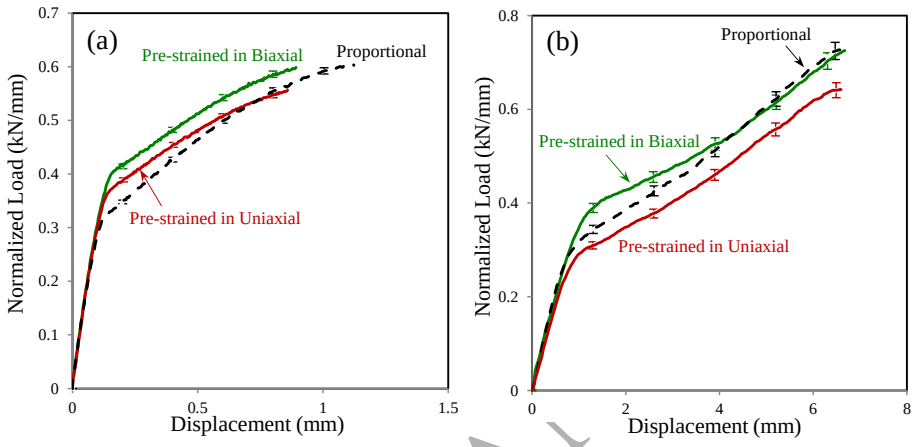

Figure 17 – Representative load-displacement responses in the RD direction of the specimens of (a) shear and (b) v-bend after pre-straining. Results of the proportional tests are also shown for comparison. Note that due to the different initial sheet thicknesses caused by pre-straining, the loads are normalized by the initial sheet thicknesses to provide a better comparison between different tests.

Table 5 – Fracture strains obtained from non-proportional tests performed with different orientations. SD stands for standard deviations.

First stage deformation	Second stage deformation	Orientation	$\mathcal{E}_1$ (SD)	$\mathcal{E}_2$ (SD)	von Mises Eq. Strain (SD)
Uniaxial tension	Shear	RD	0.20 (0.01)	-0.23 (0.01)	0.25 (0.01)
	Plane-strain	RD	0.19 (0.01)	0.00 (0.00)	0.22 (0.01)
	Plane-strain	TD	0.18 (0.01)	0.00 (0.00)	0.21 (0.02)
Eq. Biaxial Tension	Shear	RD	0.18 (0.01)	-0.23 (0.01)	0.24 (0.01)
	Plane-strain	RD	0.15 (0.01)	0.00 (0.00)	0.17 (0.01)
	Plane-strain	TD	0.14 (0.01)	0.00 (0.00)	0.16 (0.01)

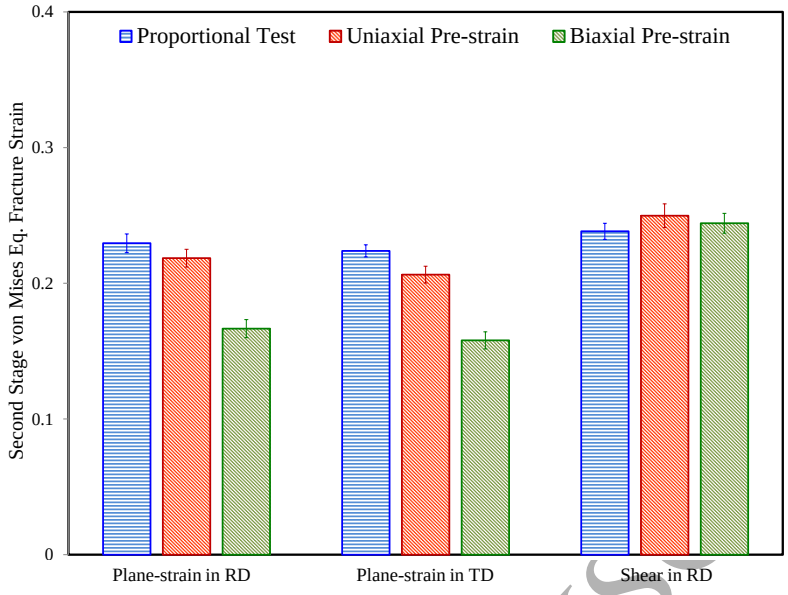

Figure 18 – Fracture strains under proportional and non-proportional tests. The pre-strains are not considered in this figure.

Moreover, the strains can be considered in a cumulative manner such as shown in Figure 19 where the strain paths of non-proportional tests from the initial deformation (pre-straining) up to fracture are compared where the abrupt changes of the stress states are apparent. In addition, the cumulative fracture strains in the non-proportional tests are compared with that of the proportional tests in Figure 20. It can be seen that the ductility under all loading conditions has increased, specifically the fracture strains of the shear tests are significantly higher due to pre-straining. The implications of the results of the non-proportional tests can be further evaluated in light of the "damage indicator" approach, as described below.

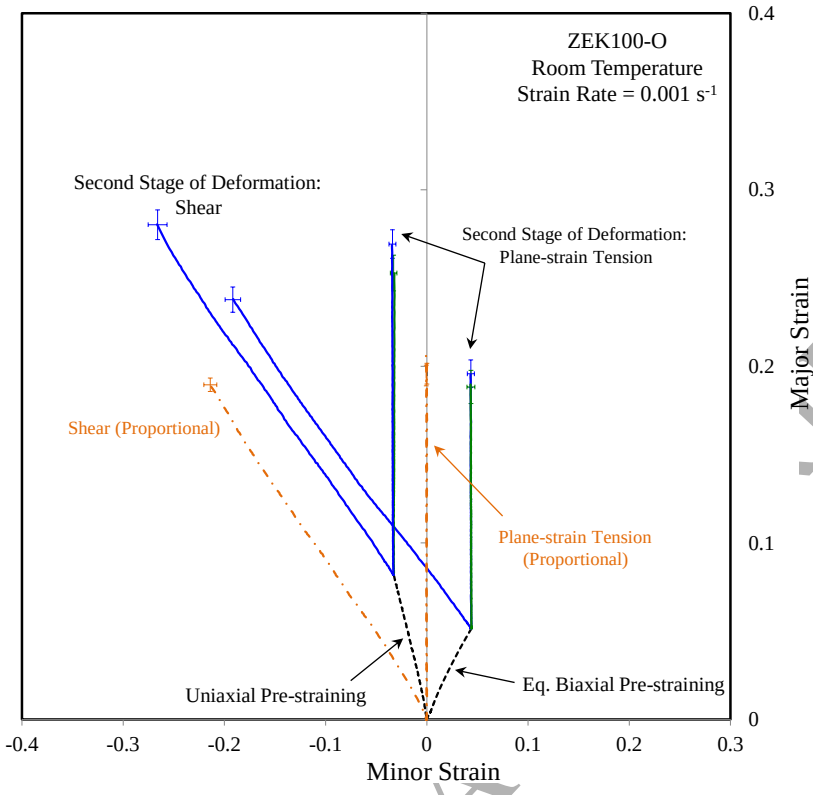

Figure 19 – Strain paths to fracture for non-proportional tests. The strain paths of the proportional tests are also shown for comparison.

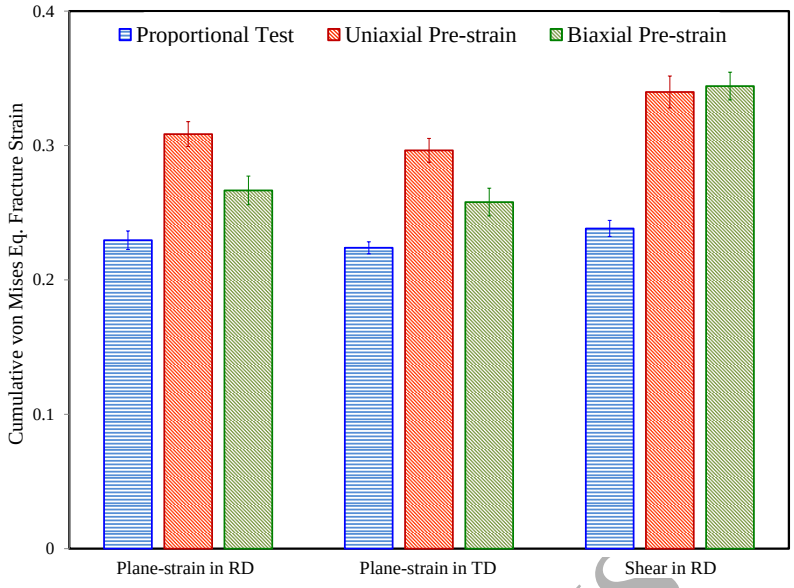

Figure 20 – Fracture strains under proportional and non-proportional tests. Here, the strains of the non-proportional tests are cumulative, *i.e.* the vertical axis plots the sum of the pre-strains plus the strains to fracture in the second stages of deformation.

4.2.1. Damage accumulation

Generally speaking, the entire class of phenomenological fracture models are built upon a failure *locus* and a damage accumulation function. Commonly, the equivalent plastic strain is taken as the failure metric and the stress state is characterized in terms of the stress triaxiality. Most of the reported work presented the results of fracture simulations in terms of averaged stress triaxiality (*e.g.* Bao and Wierzbicki, 2004) or the stress triaxiality at the onset of fracture (*e.g.* Barsoum and Faleskog, 2007). However, a more recent investigation into non-proportionality by Benzerga *et al.* (2012) raised doubts about utilizing averaged or final stress triaxialities for fracture characterization. Moreover, another common practice in the literature to consider non-proportionality is utilizing a damage parameter, *D*, in the form of:

$$D = \left[\frac{\varepsilon^p}{\varepsilon^f(\eta, \bar{\theta})} \right]^m \tag{13}$$

where ε^p is the equivalent plastic strain and *m* is the damage exponent. It is important to emphasize that the formulation in Eq. (13) is purely phenomenological and only strictly valid for

proportional loading. For the case of non-constant stress triaxiality and Lode parameter, Eq. (13) can be written in the incremental form of:

$$dD = \frac{m}{\varepsilon^f(\eta,\bar{\theta})}\left[\frac{\varepsilon^p}{\varepsilon^f(\eta,\bar{\theta})}\right]^{m-1} d\varepsilon^p \tag{14}$$

Such that the cumulative D can be obtained with the following integration:

$$D = \int \frac{m}{\varepsilon^f(\eta,\bar{\theta})}\left[\frac{\varepsilon^p}{\varepsilon^f(\eta,\bar{\theta})}\right]^{m-1} d\varepsilon^p \tag{15}$$

For the case of a linear damage accumulation with m=1.0, Eq. (15) reduces to:

$$D = \int \frac{d\varepsilon^p}{\varepsilon^f(\eta,\bar{\theta})} \tag{16}$$

Linear damage in Eq. (16) was first utilized by Johnson and Cook (1985) and is also identical to definition of the so-called "damage indicator" utilized in Marcadet and Mohr (2016). Eqs. (13-16) suggest that the damage starts to accumulate from the onset of plastic deformation up to fracture when the damage parameter D reaches unity. As shown in Figure 21, the rate of increasing D is determined by the exponent m in which slow ($m>1.0$) to fast ($m<1.0$) rates of damage (with respect to ε^p) can be obtained, and m=1.0 results in a linear damage accumulation; thus, based on Eqs. (13-16) damage accumulation is never zero with plastic deformation.

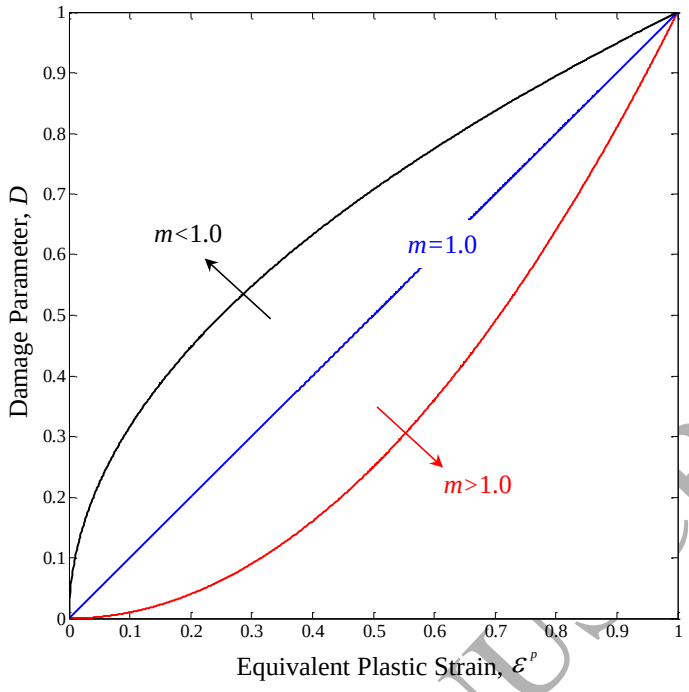

Figure 21 – Accumulation of the damage parameter, *D*, with plastic deformation for different ranges of the damage exponent.

To demonstrate the evolution of damage for the non-proportional tests performed in the present study, values of the damage parameter for some typical damage exponents used in the literature are shown in Table 6. It is evident from the results in Figure 18 that pre-straining under uniaxial or biaxial tension did not have any impact on the subsequent fracture strain under the shear state. In fact, when considering the cumulative values in Figure 20, the cumulative fracture strains are increased by the initial pre-straining. This observation is in contradiction with the approach of Eqs. (13-16) since based on Table 6, the value of *D* before the second stages of deformation is a positive value indicating the existence of an initial damage in the material before commencing the second stage of deformation. To show this discrepancy, Figure 22 compares the predicted fracture strains using different values of *m* along with the experimental data for different pre-straining conditions. The predicted fracture strains are also presented in Table 6. It can be seen from Figure 22 and Table 6 that increasing the value of the damage exponent leads to better fracture predictions for the shear state for both pre-straining conditions; however, the damage exponent of unity provides the best prediction for the plane-strain tension

test after biaxial pre-straining. It is evident from the comparison between the phenomenological model predictions and measured fracture strains that no single value of damage exponent can capture the measured trends.

Table 6 – Damage parameter *D* for different pre-straining conditions with various damage exponents and their predictions for the fracture under the second stages of deformation.

	Pre-straining type	***m*=0.5**	***m*=1.0**	***m*=1.5**
Damage parameter *D*	Uniaxial	43%	19%	8%
Damage parameter *D*	Biaxial	48%	23%	11%
Predicted shear fracture strain (%Error)	Uniaxial	0.08 (69%)	0.19 (23%)	0.23 (10%)
Predicted shear fracture strain (%Error)	Biaxial	0.06 (74%)	0.18 (25%)	0.22 (10%)
Predicted plane-strain fracture strain in RD (%Error)	Uniaxial	0.08 (66%)	0.19 (15%)	0.22 (1%)
Predicted plane-strain fracture strain in RD (%Error)	Biaxial	0.06 (65%)	0.18 (6%)	0.21 (27%)
Predicted plane-strain fracture strain in TD (%Error)	Uniaxial	0.08 (62%)	0.19 (10%)	0.22 (5%)
Predicted plane-strain fracture strain in TD (%Error)	Biaxial	0.06 (63%)	0.18 (11%)	0.21 (31%)

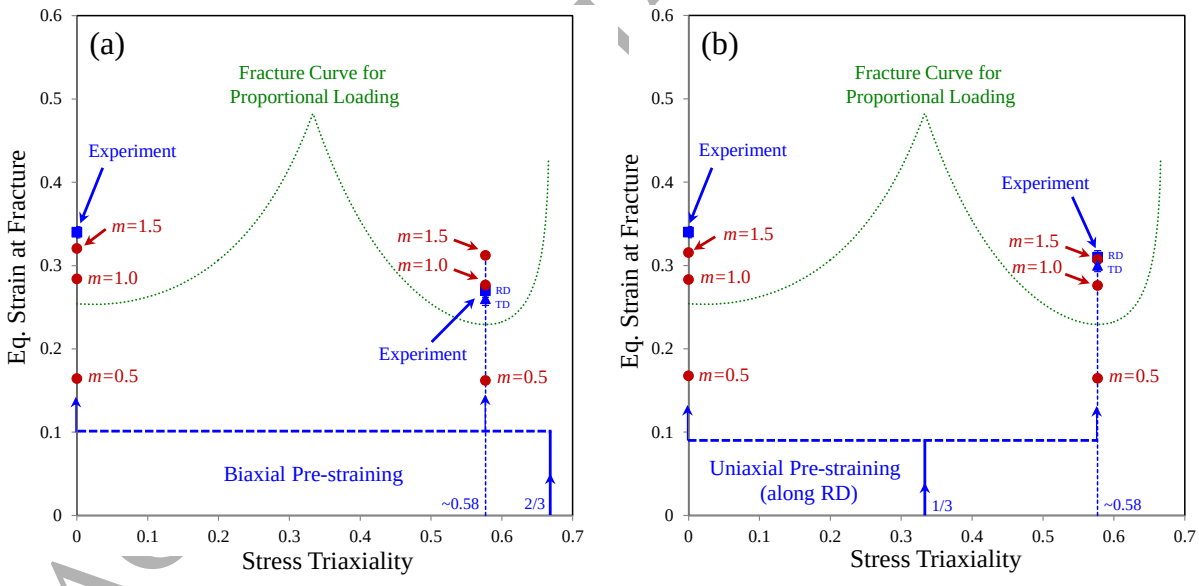

Figure 22 – Influence of the damage exponent, *m*, on non-proportional fracture predictions with (a) biaxial pre-straining and (b) uniaxial pre-straining (along RD). Load path histories are shown as blue curves. Predictions of fracture strain using the damage indicator approach for a range of damage exponents (*m* = 0.5, 1.0, 1.5) are plotted as red symbols and corresponding values of *m* are indicated. For reference, the proportional fracture *locus* in the RD is also plotted (green curve).

The results of the non-proportional tests suggest that the damage mechanisms responsible for fracture in the shear and plane-strain tension states are different such that only the damage mechanisms in the plane-strain condition were affected by pre-straining. In other words, the shear fracture response of the material after uniaxial or biaxial pre-straining is similar to the behaviour of un-deformed material, at least for the pre-straining levels considered. In addition, pre-straining prior to the plane-strain tension tests results in different impacts on the fracture strains if the initial deformation is uniaxial or biaxial tension (also note the higher damage parameters for biaxial tension in Table 6). Further investigation in this area requires the evaluation of additional stress states for both the first stage (pre-straining) and second stage of deformation to provide a more complete picture of the influence of non-proportional loading on the fracture response of the alloy. The present results highlight that phenomenological damage indicator models may not be appropriate for severe changes in strain paths. Microstructural evolutions will certainly play a role with respect to fracture in non-linear strain paths. Future work is required to connect the macroscopic fracture behavior to the underlying microscopic damage mechanisms.

5. Conclusions

Fracture experiments were performed with different types of specimens extracted from a rare-earth magnesium alloy sheet to reveal the behaviour of the material at room temperature, under quasi-static conditions. The results of proportional loading under stress states of shear, uniaxial tension, plane-strain tension, and equi-biaxial tension showed that a moderate anisotropic trend exits in the fracture response of the magnesium alloy. The plane-strain tension condition was obtained with three different types of specimens for which it was shown that the v-bend test can lead to a desired condition of almost perfectly zero minor strains. In addition, the fracture strains obtained with the v-bend test are higher than its counterparts since the maximum strains happen on the surface of the specimen with suppressed necking. Non-proportional tests were performed with uniaxial or biaxial pre-straining to the same plastic work level followed by abrupt changes of the stress state to plane-strain tension or shear. The measure of the plastic work was chosen to stop the pre-straining under different stress states to achieve an equivalent plasticity level before commencing the second stages of deformation. It was observed that fracture strains under the

shear state did not show any significant sensitivity to uniaxial or biaxial pre-straining histories, *i.e.* the shear fracture strains were similar in both the un-deformed and pre-strained sheets. Furthermore, when considering cumulative strains from the initial deformation to fracture, the ductility of the material increased under both pre-straining conditions. The novel experimental design of non-proportional experiments facilitated an analytical evaluation of using a so-called damage indicator approach where it was shown that the damage indicator approach commonly used in phenomenological fracture modelling of materials is not applicable to all stress states, at least for the material under investigation.

Acknowledgments

Financial support for this work provided by Cosma International, Automotive Partnership Canada, the Ontario Research Fund, the Natural Sciences and Engineering Research Council of Canada, the Canada Research Chairs Secretariat, and the Canada Foundation for Innovation is gratefully acknowledged. Also the authors would like to thank Dr. Michael Nemcko for helpful discussions on deformation mechanisms of magnesium alloys.

References

Abedini A, Butcher C, Anderson D, Worswick M J, Skszek T, Fracture characterization of automotive alloys in shear loading, SAE International Journal of Materials and Manufacturing, 2015, 8(3).

Abedini A, Butcher C, Nemcko M J, Kurukuri S, Worswick M J, Constitutive characterization of a rare-earth magnesium alloy sheet (ZEK100-O) in shear loading: studies of anisotropy and rate sensitivity, International Journal of Mechanical Sciences, 2017a, 128-129:54-69.

Abedini A, Butcher C, Worswick M J, Fracture characterization of rolled sheet alloys in shear loading: Studies of specimen geometries, anisotropy, and rate sensitivity, Experimental Mechanics, 2017b, 57:75-88.

Abedini A, Butcher C, Rahmaan T, Worswick M J, Evaluation and calibration of anisotropic yield criteria in shear loading: Constraints to eliminate numerical artefacts, International Journal of Solids and Structures, 2017c, http://dx.doi.org/10.1016/j.ijsolstr.2017.06.029.

Abedini A, Butcher C, Worswick M J, An evolving non-associative anisotropic-asymmetric plasticity model for magnesium alloys, submitted for possible publication, 2017d.

Anderson D, Winkler S, Bardelcik A, Worswick M J, Influence of stress triaxiality and strain rate on the failure behavior of a dual-phase DP780 steel, Materials and Design, 2014, 60:198-207.

Anderson D, Butcher C, Pathak N, Worswick M J, Failure parameter identification and validation for a dual-phase 780 steel sheet, International Journal of Solids and Structures, 2017, 124:89-107.

Bagheriasl R, Worswick M J, Formability of AA3003 brazing sheet at elevated temperatures: limiting dome height experiments and determination of forming limit diagrams, International Journal of Material Forming, 2015, 8(2):229-244.

Barlat F, Gracio J J, Lee M, Rauch E F, Vincze G, An alternative to kinematic hardening in classical plasticity, International Journal of Plasticity, 2011, 27:1309-1327.

Barlat F, Jeong Y, Ha J, Tome C, Lee M, Wen W, Advances in constitutive modeling of plasticity for forming applications, Key Engineering Materials, 2017, 725:3-14.

Bai Y, Wierzbicki T, A new model of metal plasticity and fracture with pressure and Lode dependence, International Journal of Plasticity, 2008, 24:1071-1096.

Bai Y, Wierzbicki T, Application of extended Mohr-Coulomb criterion to ductile fracture, International Journal of Fracture, 2010, 161:1-20.

Bao Y, Dependence of fracture ductility on thickness, Thin-walled Structures, 2004, 42:1211-1230.

Bao Y, Wierzbicki T, On fracture locus in the equivalent strain and stress triaxiality space, International Journal of Mechanical Sciences, 2004, 46(1):81-98.

Bao Y, Treitler R, Ductile crack formation on notched AA2024-T351 bars under compression-tension loading. Materials Science and Engineering A, 2004, A384 (1-2):385-394.

Basu S, Benzerga A A, On the path-dependence of the fracture locus in ductile fracture: Experiments, International Journal of Solids and Structures, 2015, 71:79-90.

Barsoum I, Faleskog J, Rupture mechanisms in combined tension and shear – Experiments, International Journal of Solids and Structures, 2007, 44:1769-1786.

Benzerga A A, Surovik D, Keralavarma S M, On the path-dependence of the fracture locus in ductile materials – Analysis, International Journal of Plasticity, 2012, 37:157-170.

Beese A M, Luo M, Li Y, Bai Y, Wierzbicki T, Partially coupled anisotropic fracture model for aluminum sheets, Engineering Fracture Mechanics, 2010, 77:1128-1152.

Boba, M., Butcher, C., Panahi, N., Worswick, M.J., Mishra, R., Carter, J., Formability of magnesium-rare earth alloy ZEK100 sheet at elevated temperatures, International Journal of Material Forming, 2017, 10:181–191.

Butcher C, Abedini A, Shear confusion: Identification of the appropriate equivalent strain in simple shear using logarithmic strain measure, International Journal of Mechanical Sciences, 2017, 134:273-283.

Cao T S, Gaillac A, Montmitonnet P, Bouchard P O, Identification methodology and comparison of phenomenological ductile damage models via hybrid numerical-experimental analysis of fracture experiments conducted on a zirconium alloy, International Journal of Solids and Structures, 2013, 24:3984-3999.

Cazacu O, Plunkett B, Barlat F, Orthotropic yield criterion for hexagonal closed packed metals, International Journal of Plasticity, 2006, 22:1171-1194.

Chaboche J L, A review of some plasticity and viscoplasticity constitutive theories, International Journal of Plasticity, 2008, 24:1642-1693.

Cheong K, Omer K, Butcher C, George R, Dykeman J, Evaluation of the VDA 238-100 tight radius bending tests using digital image correlation strain measurement, Journal of Physics: Conference Series, 896, 012075, 1-9.

Clift S E, Hartley P, Sturgess C E N, Rowe G W, Fracture prediction in plastic deformation processes, International Journal of Mechanical Sciences, 32:1-17.

Dunand M, Mohr D, Hybrid experimental-numerical analysis of basic ductile fracture experiments for sheet metals, International Journal of Solids and Structures, 2010, 47:1130-1143.

Dunand M, Mohr D, Optimized butterfly specimen for the fracture testing of sheet materials under combined normal and shear loading, Engineering Fracture Mechanics, 2011, 78:2919-2934.

Flores P, Tuninetti V, Gilles G, Gonry P, Duchene L, Habraken A M, Accurate stress computation in plane strain tensile tests for sheet metal using experimental data, Journal of Material Processing Technology, 2010, 210:1772-1776.

Graf A, Hosford W F, Effect of changing strain paths on forming limit diagrams of aluminum 2008-T4. Metallurgical Transactions, 1993, 24:2503-2512.

Guo X Q, Wu W, Wu P D, Qiao H, An K, Liaw P K, On the Swift effect and twinning in a rolled magnesium alloy under free-end torsion, Scripta Materialia, 2013, 69:319-322.

Gurben G, Hopperstad O S, Borvik T, Evaluation of uncoupled ductile fracture criteria for dual-phase steel Docol 600DL, International Journal of Mechanical Sciences, 2012, 62:133-146.

Hotz W, Timm J, Experimental determination of forming limit curves (FLC). Proceedings of the 7th Numisheet Conference, 2008, 271-278.

Imandoust A, Barrett C D, Al-Samman T, Inal K A, El Kadiri H, A review of the effect of rare-earth elements on texture evolution during processing of magnesium alloys, Journal of Materials Science, 2017, 52:1-29.

Jia Y, Bai Y, Experimental study on the mechanical properties of AZ31B-H24 magnesium alloy sheets under various loading conditions, International Journal of Fracture, 2016, 197:25-48.

Jocham D, Gaber C, Bottcher O, Wiedemann P, Volk W, Experimental prediction of sheet metal formability of AW-5754 for non-linear strain paths by using a cruciform specimen and a blank holder with adjustable draw beads on a sheet metal testing machine, International Journal of Material Forming, 2016, DOI 10.1007/s12289-016-1304-9.

Johnson G R, Cook W H, Fracture characteristics of three metals subjected various strains, strain rates, temperatures and pressures, Engineering Fracture Mechanics, 1985, 21(1):31-48.

Koc M, Billur E, Cora O N, An experimental study on the comparative assessment of hydraulic bulge test analysis and methods, Materials and Design, 2011, 32:272-281.

Kofiani K, Nonn A, Wierzbicki T, New Calibration method for high and low triaxiality and validation on SENT specimens of API X70, International Journal of Pressure Vessels and Piping, 2013, 111-112:187-201.

Korkolis Y P, Kyriakides S, Path-dependent failure of inflated aluminum tubes, International Journal of Plasticity, 2009, 25:2059-2080.

Kurukuri S, Worswick M J, Bardelcik A, Mishra R K, Carter J T, Constitutive behavior of commercial grade ZEK100 magnesium alloy sheet over a wide range of strain rates. Metallurgical and Materials Transactions A, 2014, 45:3321-3337.

Kurukuri S, Worswick M J, Ghaffari Tari D, Mishra R K, Carter J T, Rare-sensitivity and tension-compression asymmetry in AZ31B magnesium alloy sheet, Philosophical Transactions of the Royal Society A, 2014, 372:20130216.

Lian J, Sharaf M, Archie F, Munstermann S, A hybrid approach for modelling of plasticity and failure behaviour of advanced high-strength steel sheets, International Journal of Damage Mechanics, 2013, 22(2):188-218.

Lou Y, Yoon J W, Anisotropic ductile fracture criterion based on linear transformation, International Journal of Plasticity, 2017, 93:3-25.

Luo M, Dunand M, Mohr D, Experimental and modeling of anisotropic extrusions under multi-axial loading – Part II: ductile fracture, International Journal of Plasticity, 2012, 32:36-58.

Lou Y, Huh H, Extension of a shear-controlled ductile fracture model considering the stress triaxiality and the Lode parameter, International Journal of Solids and Structures, 2013, 50:447-455.

Mahmudi R, A novel technique for plane-strain tension testing of sheet metals, Journal of Material Processing Technology, 1999, 86:237-244.

Malcher L, Andrade Pires F M, Cesar de Sa J M A, An assessment of isotropic constitutive models for ductile fracture under high and low stress triaxiality, International Journal of Plasticity, 2012, 30:81-115.

Marcadet S J, Mohr D, Effect of compression-tension loading reversal on the strain to fracture of dual phase steel sheets, International Journal of Plasticity, 2015, 72:21-43.

Marcadet S J, Mohr D, Critical hardening rate model for predicting path-dependent ductile fracture, International Journal of Fracture, 2016, 200:77-98.

Mohr D, Henn S, Calibration of stress-triaxiality dependent crack formation criteria: A new hybrid experimental-numerical method, Experimental Mechanics, 2007, 47:805-820.

Mohr D, Marcadet S, Micromechanically-motivated phenomenological Hosford-Coulomb model for predicting ductile fracture initiation at low stress triaxialities, International Journal of Solids and Structures, 2015, 67-68:40-55.

Morales-Palme D, Vallellano C, Garcia-Lomas F, Assessment of the effect of the through-thickness strain/stress gradient on the formability of stretch-bend metal sheets, Materials and Design, 50:798-809.

Omer K, ten Kortenaar L, Butcher C, Worswcik M J, Malcolm S, Detwiler D, Testing of a hot stamped axial crush member with tailored properties – Experiment and models, International Journal of Impact Engineering, 2017, 103:12-28.

Oyane M, Sato T, Okimoto K, Shima S, Criterion for ductile fracture and their applications, Journal of Mechanical Working Technology, 1980, 4:65-81.

Papasidero J, Doquet V, Mohr D, Ductile fracture of aluminum 2024-T351 under proportional and non-proportional multi-axial loading: Bao-Wierzbicki results revisited International Journal of Solids and Structures, 2015, 69-70:459-474.

Pathak N, Butcher C, Worswick M J, Bellhouse E, Gao J, Damage evolution in complex-phase and dual-phase steels during edge stretching, Materials, 2017, 10(4):1944-1996.

Peirs J, Verleysen P, Degrieck J, Novel technique for static and dynamic shear testing of Ti6Al4V sheet. Experimental Mechanics, 2012, 52:729-741.

Rahmaan T, Abedini A, Butcher C, Pathak N, Worswick M J, Experimental investigation of strain rate effect on fracture characteristics of DP600 and AA5182-O sheet metal alloys under shear loading, International Journal of Impact Engineering, 2017, 108:303-321.

Ray A K, Wilkinson D S, The effect of microstructure on damage and fracture in AZ31B and ZEK100 magnesium alloys, Materials Science and Engineering A, 2016, 658:33-41.

Reu P, The art and application of DIC, virtual strain gage size study, Experimental Techniques, 2015, 39:1-3.

Rousselier and Lou, A fully coupled void damage and Mohr-Coulomb based ductile fracture model in the framework of a reduced texture methodology. International Journal of Plasticity, 2014, 55:1-24.

Roth C C, Mohr D, Ductile fracture experiments with locally proportional loading histories, International Journal of Plasticity, 2016, 79:328-354.

Scales M, Tardif N, Kyriakides S, Ductile fracture of aluminum alloy tubes under combined torsion and tension, International Journal of Solids and Structures, 2016, 97-98:116-128.

Steglich D, Tian X, Bohlen J, Kuwabara T, Mechanical testing of thin sheet magnesium alloys in biaxial tension and uniaxial compression, Experimental Mechanics, 2014, 54:1247-1258.

Stoughton T B, A general forming limit criterion for sheet metal forming, International Journal of Mechanical Sciences, 2000, 42:1-42.

Stoughton T B, Yoon J W, Path independent forming limits in strain and stress spaces, International Journal of Solids and Structures, 2012, 49:3616-3625.

Swift H, Length changes in metals under torsional overstrain, Engineering, 1947, 163:253-257.

Tarigopula V, Hopperstad O S, Langseth M, Clausen A H, Hild F, Lademo O G, Eriksson M, A study of large plastic deformations in dual phase steel using digital image correlation and FE analysis, Experimental Mechanics, 2008, 48:181-196.

ten Kortenaar, Failure characterization of hot formed boron steels with tailored mechanical properties, M.Sc. Thesis, 2016, University of Waterloo.

Volk W, Suh J, Prediction of formability for non-linear deformation history using generalized forming limit concepts (GFLC), AIP Conference Proceedings, 2013, 1567:556-561.

Wang K, Greve L, Wierzbicki T, FE simulation of edge fracture considering pre-damage from blanking, International Journal of Solids and Structures, 2015, 71:206-218.

Yoshida K, Kuwabara T, Effect of strain hardening behavior on forming limit stresses of steel tubes subjected to nonproportional loading paths, International Journal of Plasticity, 2007, 23:1260-1284.

Zarandi F, Yue S, Magnesium sheet; challenges and opportunities, Magnesium alloys - design, processing and properties, Frank Czerwinski (Ed.), 2011. ISBN: 978-953-307-520-4.